Contribution of Intraseasonal Variability to Uncertainty in Simulating Seasonal Activity of Northwest Pacific Tropical Cyclones as Demonstrated Using 1998

RUIFEN ZHAN,[a,f] JIUWEI ZHAO,[b] YUQING WANG,[c] DAEHYUN KIM,[d] JONG-SEONG KUG,[d] CHAO LIU,[d] AND YINGXIA GAO[e]

[a] *Department of Atmospheric and Oceanic Sciences & Institute of Atmospheric Sciences, CMA-FDU Joint Laboratory of Marine Meteorology, Fudan University, Shanghai, China*
[b] *Collaborative Innovation Center on Forecast and Evaluation of Meteorological Disasters, Institute of Climate and Application Research, Nanjing University of Information Science & Technology, Nanjing, China*
[c] *Department of Atmospheric Sciences and International Pacific Research Center, School of Ocean and Earth Science and Technology, University of Hawai'i at Mānoa, Honolulu, Hawaii*
[d] *School of Earth and Environmental Sciences, Seoul National University, Seoul, South Korea*
[e] *School of Ecology and Environment, Inner Mongolia University, Hohhot, China*
[f] *Key Laboratory of Straits Severe Weather China Meteorological Administration, Fuzhou, China*

(Manuscript received 4 October 2024, in final form 13 March 2025, accepted 24 April 2025)

ABSTRACT: What causes the uncertainty in simulations of seasonal tropical cyclone (TC) activity remains unclear. Here, we uncovered the important contribution of intraseasonal variability to the uncertainty in simulating TC genesis frequency (TCGF) over the western North Pacific (WNP). This is demonstrated by analyzing 50-member ensemble simulations for the period June–November in 1998 using a high-resolution regional climate model. The uncertainty spans from +1 to −1.75 standard deviations (STDs), considerably larger than the observed deviation of −1.5 STDs. The uncertainty in simulations stems from two atmospheric dynamic modes, namely, the monopole and dipole modes. The monopole mode is characterized by a basin-uniform anomalous circulation pattern and controls TC genesis over the whole WNP, while the dipole mode is marked by a zonal dipole of circulation anomalies and redistributes TC genesis locations among the ensemble members. Both modes are dominated by the intraseasonal variability, accounting for over 62% of the total uncertainty in the simulated TCGF. The intraseasonal variability observed over the WNP in 1998 was relatively weak, leading to significant uncertainty in simulating intraseasonal variability east of the Philippines among the ensemble members, which in turn caused uncertainty in the simulation of TCGF. By conditionally constraining the intensity of intraseasonal variability, we can significantly reduce model uncertainties in simulating TCGF. The finding provides new insights into understanding the simulation uncertainty and predictability of seasonal TC activity over the WNP.

KEYWORDS: Tropical cyclones; Uncertainty; Climate models; Intraseasonal variability

1. Introduction

The western North Pacific (WNP), a region witnessing approximately one-third of the world's tropical cyclone (TC) genesis frequency (TCGF), stands as the most active basin of TC activity in the world (Huang et al. 2023). Over the past decades, advancements of high-resolution climate models have steadily improved their capability to simulate WNP TC activity across various time scales, from synoptic to seasonal, interannual, and beyond (Zhao et al. 2009, 2015; Jiang et al. 2016; Ahn et al. 2020; Si et al. 2024; Wang et al. 2025). Despite considerable progress, the fidelity of simulating and predicting TC activity at subseasonal to seasonal (S2S) time scales remains challenging (Schreck 2023). This challenge underscores the imperative efforts for a deeper comprehension of the pertinent dynamics of predictability on the S2S time scale (Xiang et al. 2022). Therefore, it is crucial to identify the sources of uncertainty in simulations of seasonal TC activity.

Currently, high-resolution atmospheric and coupled general circulation models are commonly employed to simulate seasonal TC activity. These models generally capture the climatological distributions and seasonal variability of key TC metrics, such as genesis frequency, track density, and intensity over the WNP and other basins (Emanuel 2010; Knutson et al. 2019; Patricola et al. 2016; Mei and Li 2022; Li and Mei 2024; Murakami et al. 2011, 2015). Besides general circulation models, regional climate models have also been frequently utilized (Knutson et al. 2008; Zhan et al. 2011; Zhang and Wang 2017, 2018; Shen et al. 2017, 2019). These models with finer resolution excel in capturing both the synoptic evolution of TCs and the interannual variability of TCGF over the WNP.

However, there has been a considerable body of literature arguing that climate modeling exhibits large uncertainty in simulating TCGF (e.g., Wu et al. 2012; Camargo and Wing 2016; Song et al. 2022; Zhao et al. 2023a). Fully coupled models, while offering a nuanced representation of the complex interactions within the climate systems, often harbor systematic biases in climate mean states and associated internal climate variabilities (Wang et al. 2014). These biases, particularly in representing phenomena like El Niño–Southern Oscillation (ENSO; Jin 1997; Ham and Kug 2015), Atlantic multidecadal oscillation (AMO; Trenberth and Shea 2006; Zhang et al. 2018), and interdecadal Pacific oscillation (IPO; Henley et al. 2015; Zhao et al. 2018),

Corresponding author: Jiuwei Zhao, jiuwei@nuist.edu.cn

DOI: 10.1175/JCLI-D-24-0544.1

© 2025 American Meteorological Society. This published article is licensed under the terms of the default AMS reuse license. For information regarding reuse of this content and general copyright information, consult the AMS Copyright Policy (www.ametsoc.org/PUBSReuseLicenses).

Unauthenticated | Downloaded 11/13/26 12:23 PM UTC

critically degrade models' performance in simulating TC activity over the WNP. Atmospheric models, which fix the internal variability of the ocean, could still fail to simulate accurately TC activity. It is because these simulations are likely to skew the depiction of the simulated local circulations, such as the western Pacific subtropical high and monsoon circulations, thereby lowering the confidence in current TC simulations as well as future TC projections (Huang et al. 2020; Yang et al. 2020; Chen et al. 2022; Feng et al. 2023). A recent study (Zhao et al. 2023a) further demonstrated that these low confidences stem from typical atmospheric dynamic modes, such as the Pacific–Japan pattern (Huang and Li 1989; Nitta 1989) and Matsuno–Gill pattern (Gill 1980; Showman and Polvani 2010). These studies highlight the complicated interplay between small perturbations and the overarching atmospheric circulation.

On S2S time scales, boreal summer intraseasonal oscillations (BSISOs) have been identified as pivotal factors affecting WNP TCGF (Fu and Hsu 2011; Lee et al. 2013; Qian et al. 2019). These modes, through their modulation of large-scale circulation anomalies, play an important role in shaping the spatial and temporal distribution of TC genesis over the WNP (Zhang et al. 2023). Therefore, a misrepresentation of BSISO events in models is more likely to cause large simulation biases of circulation anomalies, and thus TCGF. More importantly, the BSISO characterized by northward propagation usually interacts with the background summer monsoon circulation. As a result, the associated processes could feed back to the seasonal mean Pacific–Japan mode (Lu and Lin 2009; Li et al. 2019; Zhao et al. 2023a), the subtropical high (Huang and Li 1989), and the low-level anticyclonic circulation over the WNP (Wang et al. 2021). This implies that the simulation biases can destabilize internal dynamical modes, exacerbating them through positive feedback processes and further contributing to the uncertainty in TC simulations.

The impact of subseasonal dynamical modes on WNP cyclogenesis has been well recognized (Camargo et al. 2019; Hsu et al. 2020). Recently, a study has shown that the long-standing BSISO-like circulation contributed about half of the record-low TC activity in the early summer of 2020 (Liu et al. 2021), suggesting a potential critical role of subseasonal dynamical mode in modulating seasonal TC activity. However, a systematic examination of their contribution to uncertainty in seasonal TC simulations is lacking. In this study, a 50-member ensemble simulation using a Regional Climate Model (RegCM) is used to investigate the uncertainty induced by intraseasonal variability and to quantify the contributions of the bias in the simulated intraseasonal variability to the seasonal-mean TCGF over the WNP. The use of a regional model enables us to isolate regional sources of uncertainty by excluding potential remote effects that may arise in global models. Moreover, 50 members allow us to extract the robust intrinsic modes of uncertainty. The remainder of the article is organized as follows: Section 2 introduces the data and methodology. Section 3 examines the uncertainty in simulated TCGF over the WNP. Section 4 identifies atmospheric modes responsible for the uncertainty. The contribution of intraseasonal variability to uncertainty in the simulated TCGF is evaluated in section 5. Section 6 discusses uncertainty in intraseasonal variability and its potential sources. The final section outlines the conclusions.

2. Data and methodology

a. TC and reanalysis data

In this study, the WNP TC best track dataset during 1993–2022 was derived from the Joint Typhoon Warning Center (JTWC; Knapp et al. 2010, 2018), which includes information on TC center position (longitude and latitude) and intensity (maximum sustained surface wind speed) at 6-hourly intervals. We considered a TC formation as its intensity reaches 35 kt (1 kt $\approx$ 0.51 m s^{-1}) (about 18 m s^{-1}) for the first time over the WNP. The TC season was defined for the 6 months from June to November (JJASON). We chose the period 1993–2022 for a 30-yr long time, often used to infer a climatology.

The 6-hourly atmospheric reanalysis data in the same period, mainly including sea level pressure (SLP), winds, specific humidity, and temperature at standard pressure levels with a horizontal resolution of 2.5°, were obtained from the National Centers for Environmental Prediction/National Center for Atmospheric Research Reanalysis I (NCEP/NCAR R1; Kalnay et al. 1996). The daily Optimum Interpolation SST (OISST) dataset with a horizontal resolution of 0.25° was obtained from the National Oceanic and Atmospheric Administration (NOAA; Huang et al. 2017, 2021). These data served as the foundational inputs for both the initial condition and the lateral and lower boundary conditions of the regional climate model, as well as the analysis of intraseasonal variability in observations.

b. Model experiments

In this study, we used the RegCM developed at the International Pacific Research Center (IPRC) of Hawaii University at Manoa (Wang et al. 2003). This model, originating from the high-resolution TC model, version 3 (TCM3; Wang 2001), incorporates a modified Tiedtke (Tiedtke 1989) convective parameterization scheme and a sophisticated radiation scheme; both are crucial for accurate climate simulations. Especially, the Tiedtke scheme is considered as a skilled parameterization to represent the intraseasonal variability (Liu et al. 2005; Fu et al. 2013). The model domain of the designed experiments in this study covers the whole WNP (90°E–170°W, 10°S–50°N), including a buffer zone of 5° on each side to ensure a smooth transition from driving fields to the regional model simulations. It is finely optimized at the 0.25° horizontal resolution with 28 vertical levels, which can explicitly simulate TC-like vortices. This model has demonstrated good performance in simulating seasonal activity of WNP TCs (Zhan et al. 2011; Wu et al. 2012).

Our control run using the RegCM spans from 0000 UTC 15 May each year to the end of November during 1993–2022, with the atmospheric initial and boundary conditions from NCEP/NCAR and SSTs from OISST at 6-h intervals. Notably, there is the largest positive bias in the simulated TCGF for 1998, in which there were unusually few TCs in observation over the WNP. To address the significant bias, we initiated a large ensemble run by introducing small perturbations to the initial and lateral boundary conditions [about 10^{-3} of

Unauthenticated | Downloaded 11/13/26 12:23 PM UTC

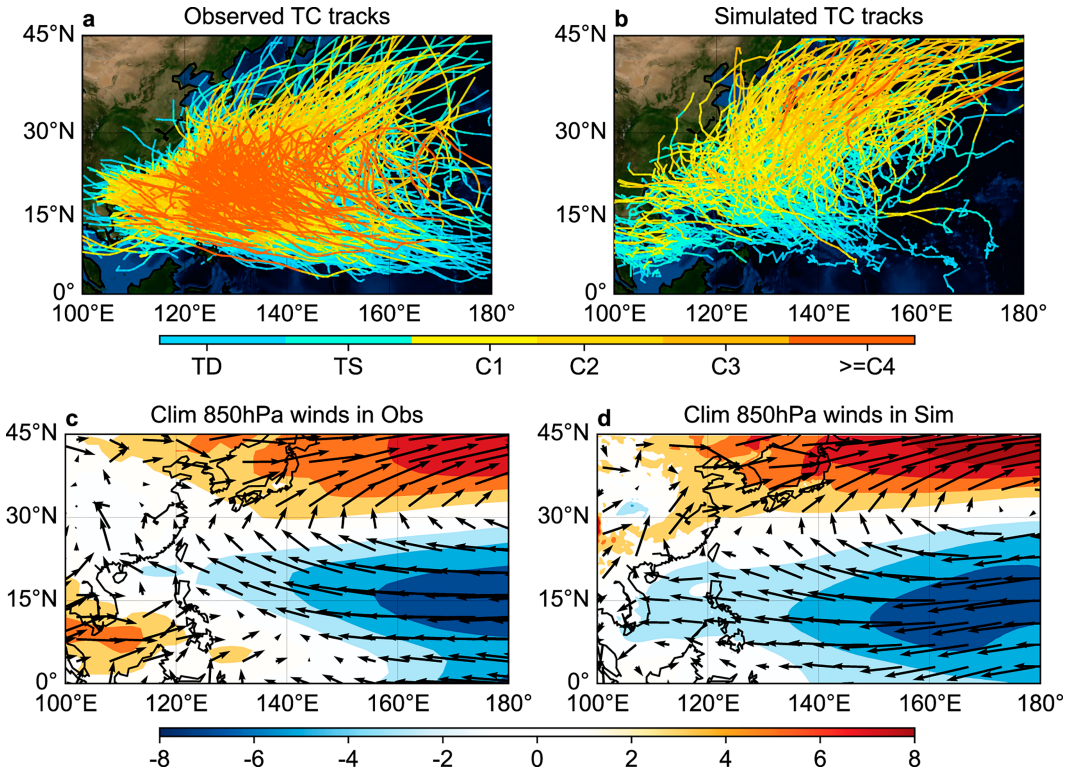


FIG. 1. (top) TC tracks and (bottom) climatological mean 850-hPa winds during JJASON from 1993 to 2022 derived from (left) observation and (right) simulations in control run. Shadings in (c) and (d) indicate the zonal wind speeds (m s^{-1}).

the standard deviation (STD) for each variable at different vertical levels] to generate 50 ensemble members for the year 1998. Note that 50 ensemble members were run to reduce sampling noise and allow subtraction of the robust uncertainty modes, since previous studies (Mei et al. 2019) have unraveled that it is best to use 25 or more ensemble members to identify internal variability/uncertainty in climate simulations. Although it is better to perform large ensemble simulations for all seasons during 1993–2022 to demonstrate the robustness of findings from a single-season simulation, considering the immense computational demands, we only conducted a large ensemble simulation for the TC season of 2009, which shows minimal bias in control run. A comparative analysis of 1998 and 2009 (section 6) demonstrates that intraseasonal variability is the main source of model predictability. The 6-hourly output from each experiment is analyzed for the TC season during June–November.

c. TC detection algorithm

The extraction of TC information from the RegCM output was facilitated using the TC detection algorithm (Zhao et al. 2009; Murakami et al. 2015). The basic extraction criteria and steps are as follows: First, there appears a low pressure center at the sea surface. Considering the initial asymmetry and weakness of TC-like vortices, the surface isobars do not need to be closed. Second, for the vortex classified as a TC, the 850-hPa wind speed should be no less than 17 m s^{-1} and the 850-hPa relative vertical vorticity should be greater than 5×10^{-5} s^{-1}. Third, to ensure a warm-core structure, the temperature averaging between 300 and 500 hPa within 1200 km of the detected vortex center must be higher than that in the annular area of 1200–2400 km. Finally, the vortex lifespan must persist at least for 2 days.

d. Extraction of model uncertainty

The empirical orthogonal function (EOF) analysis was used to extract the simulation uncertainty with a focus on the 850-hPa winds in the large ensemble runs. We first subtracted the ensemble-mean zonal and meridional winds at 850 hPa during JJASON from each of the 50 ensemble members to obtain the low-level wind (LLW) anomalies. The seasonal average of the LLW anomalies during JJASON of each ensemble member was treated as the spatial dimension, and the 50 ensemble members were treated as the temporal dimension for the EOF analysis. Based on this, we can obtain the first two EOF leading modes, namely, the dipole and monopole modes (see section 4). To quantify the simulation uncertainty induced by the two dynamic modes, we projected the 6-hourly LLW anomalies onto the LLW patterns of the two atmospheric dynamic modes following Zhao et al. (2023b), respectively, to generate a set of the corresponding principal components (PCs). Subsequently, we extracted the intraseasonal components from the PCs using a 20–90-day bandpass filter. We also conducted the EOF analysis on the bandpass-filtered 6-hourly

Unauthenticated | Downloaded 11/13/26 12:23 PM UTC

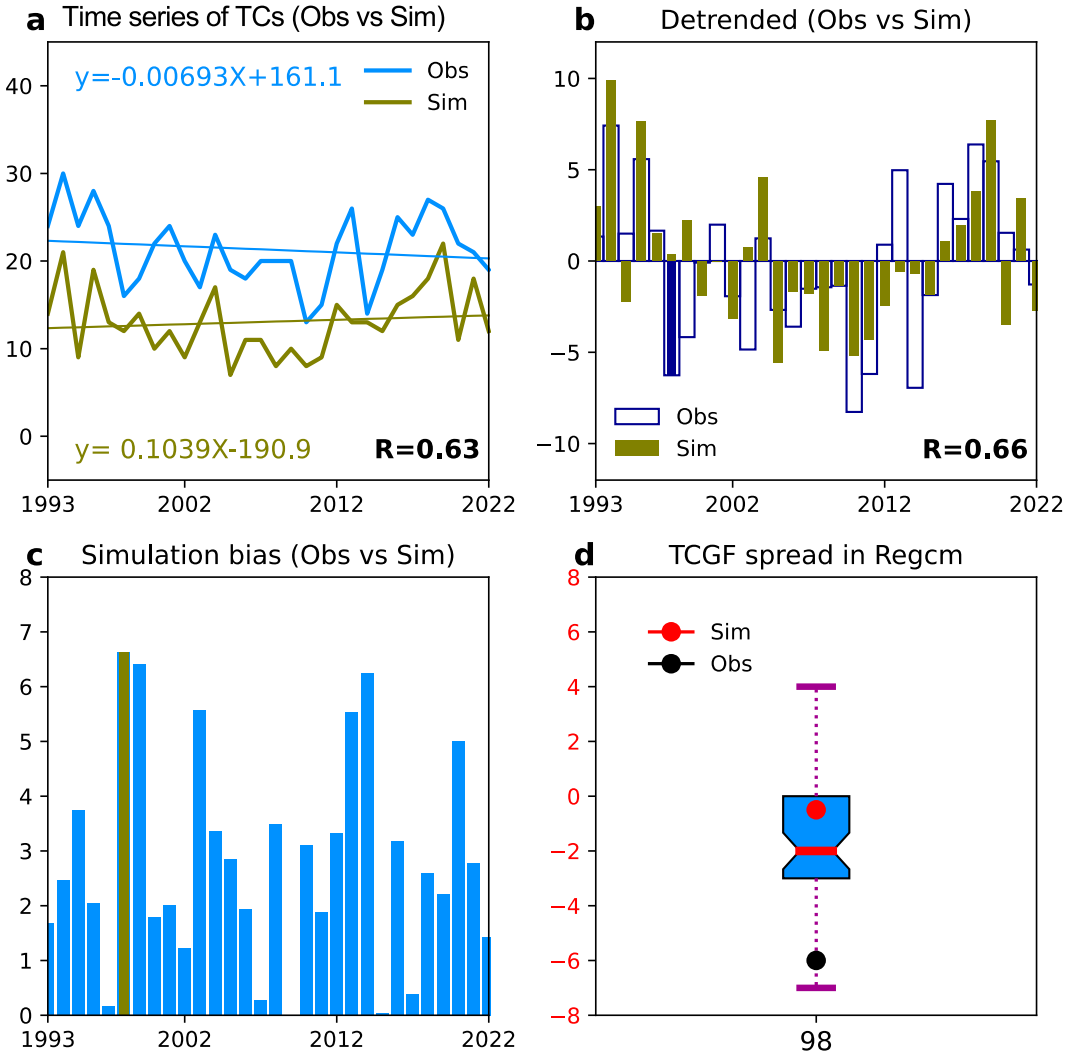


FIG. 2. (a),(b) Time series of the observed and simulated annual TCGFs from 1993 to 2022, (c) simulation biases from 1993 to 2022, and (d) the simulation spread in 1998. (a) Original and (b) detrended TCGFs in observation (dodger blue) and simulation (brown), (c) the biases of TCGF between observation and simulation based on the detrended data during 1993–2022, and (d) the spread of simulated TCGFs among 50 ensemble runs for 1998. The equations in (a) describe the best-fit linear trends (lines) for observed and simulated TCGFs with their correlation coefficient (r = 0.63) marked in the right corner; in (b), the correlation coefficient (r = 0.66) stands for the correlation between detrended time series, the blue bar shows the year 1998 from the control run, and the cyan shading represents the absolute difference in detrended TCGFs between the simulated and observed. The red (black) dot in (d) represents the simulated (observed) TCGF anomaly, and the box-and-whiskey plot stands for the maximum, minimum, medium, and 25% and 75% percentiles of TCGF anomalies based on the 50-member ensemble simulations, respectively.

LLW from the reanalysis to examine whether the reanalysis data can reproduce these two dynamic modes in 1998.

The projection method is based on the EOF analysis. Here, the EOF analysis can be expressed as

$$\mathrm{Wind}(x, y, t) = \mathrm{SP}(x, y, m) \times \mathrm{PC}(m, t), \quad (1)$$

$$\mathrm{PC}_p(m, t) = \mathrm{SP}(x, y, m)^{\mathrm{T}} \times \mathrm{Wind}(x, y, t)_p. \quad (2)$$

Here, Wind(x, y, t) represents the three-dimensional original data with x, y, and t for longitude, latitude, and time, respectively; SP(x, y, m) is the spatial patterns (e.g., monopole and dipole modes) with m representing different modes; and PC(m, t) are the principal components. For the projection, we keep the spatial pattern unchanged and get the projected PCs [$\mathrm{PC}_p(m, t)$] from a new wind field [$\mathrm{Wind}(x, y, t)_p$; the ensemble members].

3. The derived uncertainty as represented by spread of simulated TCGF

TC tracks and climatological mean 850-hPa winds during JJASON from 1993 to 2022 derived from observation and

Unauthenticated | Downloaded 11/13/26 12:23 PM UTC

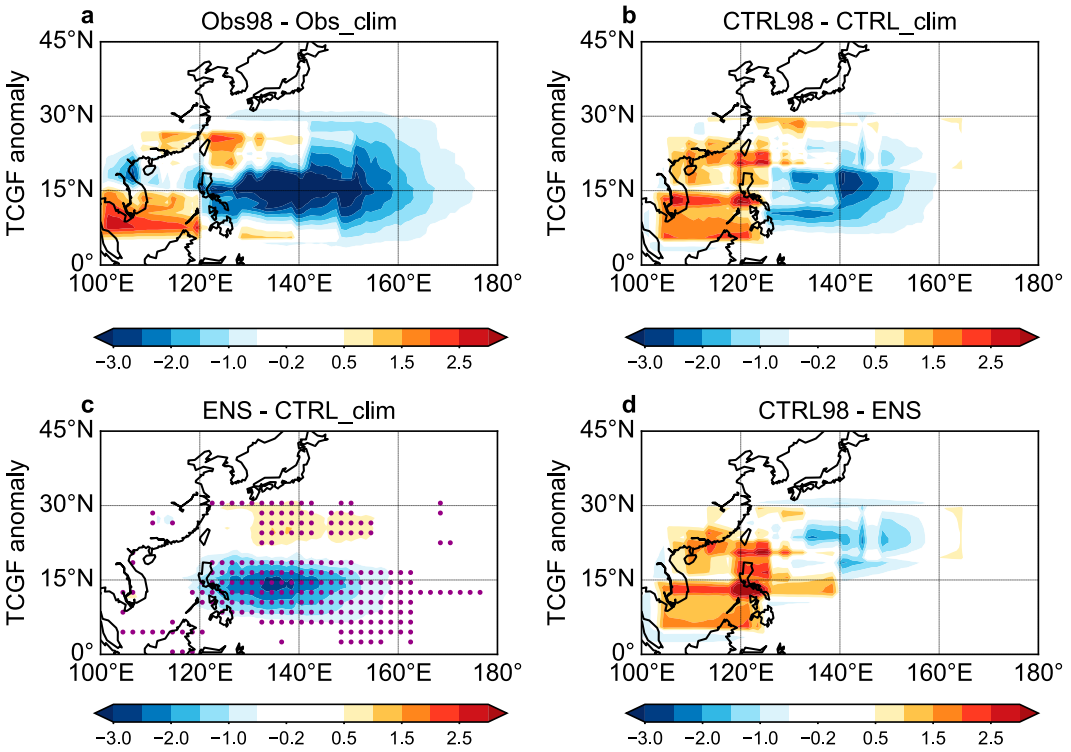


FIG. 3. Observed and simulated TCGF anomalies in 1998. (a) The observed TCGF anomalies in 1998, (b) the simulated TCGF anomalies in 1998 from the control run, (c) the difference between 50-member ensemble mean in 1998 and simulated climatological mean during 1993–2022, and (d) the difference between the control run in 1998 and the 50-member ensemble mean in 1998. The dots in (c) represent areas statistically significant above the 90% confidence level based on the Student's *t* test. The "Obs98" means the observed TCGF in 1998, while the "Obs_clim" indicates the climatological mean between 1993 and 2022; the "CTRL98" means the TCGF of 1998 in "CTRL" run, while the "CTRL_clim" represents the climatological mean of TCGF from 1993 to 2022 in "CTRL" simulations; and the "ENS" means the ensemble average of 50 members in 1998.

simulations using the RegCM, respectively, are shown in Fig. 1. We can see that the RegCM generally reproduces the observed TC tracks, albeit a systematic bias over the southeastern part of the WNP and the South China Sea (SCS) as well as an overall weaker intensity in simulations. These discrepancies are potentially attributed partly to the weaker and westward displaced monsoon trough (Huangfu et al. 2017; Feng et al. 2023) in the simulations (Figs. 1c,d) and partly to the relatively coarse model resolution (Roberts et al. 2020).

Figures 2a and 2b show the time series of the observed and simulated annual TCGFs from 1993 to 2022. The RegCM captures the realistic interannual variability of TCGF during 1993–2022, with a correlation coefficient of 0.63 between the observed and the simulated TCGF, significant at the 99% confidence level (Fig. 2a). Note that some disagreements exist with a large low bias in the climatological mean of TCGF and with a weak increasing long-term trend instead of a weak decreasing long-term trend in the observations (Fig. 2a). With the long-term trends removed, the correlation coefficient increases to 0.66 (Fig. 2b), suggesting that the model reproduced reasonably the interannual variability. Moreover, the variances of the simulated and observed TCGF are comparable, with one STD accounting for about four TCs. However, the model did not consistently reproduce the observed TCGF each year. Especially, the 1998 simulation in the control run exhibits the largest bias during the past 30 years (Fig. 2c), namely, the model simulated a nearly neutral condition in 1998, which is in contrast to the observed substantially below-normal condition (about −1.5 STD). The unusually low TCGF observed in 1998 has been attributed to the development of a typical La Niña event following the super El Niño of 1997 (Zhan et al. 2017). The model bias in the simulated TCGF for 2009 is minimal, which was an El Niño year.

Given the substantial simulation bias for the unusually inactive TC activity in 1998, we conducted 50-member ensemble simulations by randomly and minutely perturbating the initial and boundary conditions for SLP, winds, temperatures, humidities, and SSTs to examine the source of simulation uncertainty (see section 2). The spread of the simulated TCGF in 1998 among the 50-member ensemble runs is shown in Fig. 2d. The control run for 1998 simulated 11 TCs during JJASON, close to the simulated climatological mean of 12 TCs during 1993–2022. The large ensemble mean indicates a below-normal condition with about 10 TCs, a deviation of 0.5 STD below the simulated climatological mean. At the same time, the spread of large ensemble simulations ranged from +1 STD (16 TCs) to −1.75 STDs

Unauthenticated | Downloaded 11/13/26 12:23 PM UTC

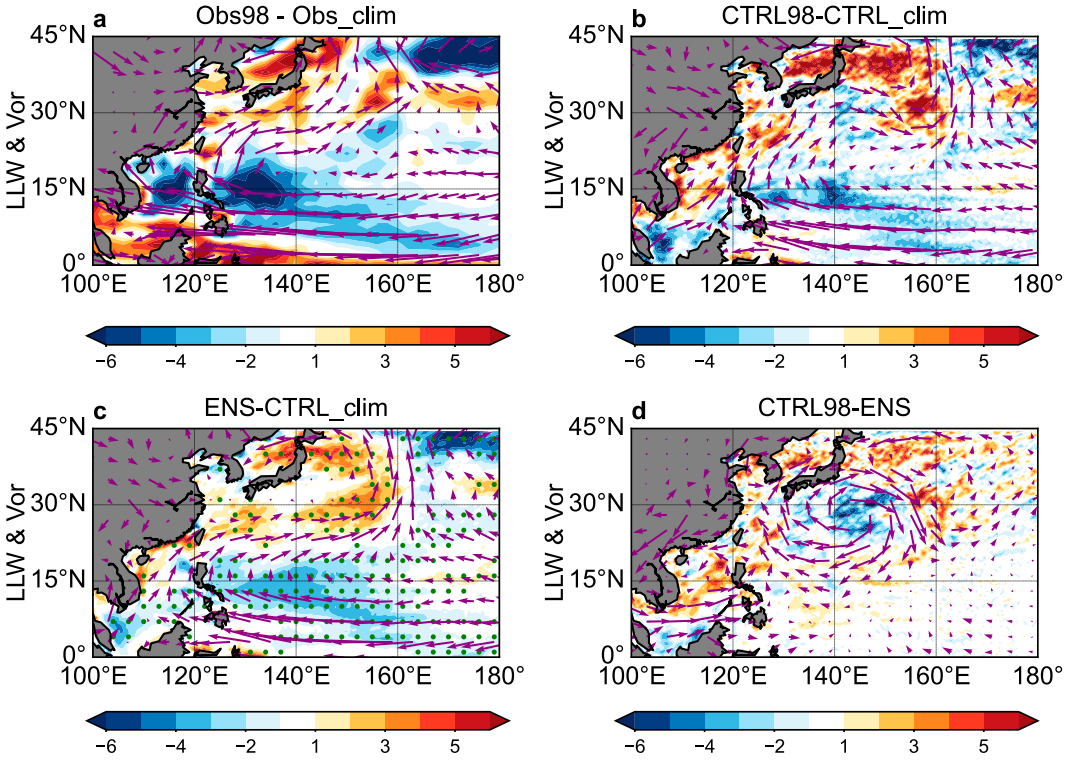


FIG. 4. The 850-hPa wind (vector; m s^{-1}) and vorticity (shade; 10^{-6} s^{-1}) anomalies in reanalysis, climate and large ensemble runs in 1998. (a) The observed, (b) the simulated, (c) the difference between 50-member ensemble mean in 1998 and simulated climatological mean during 1993–2022, and (d) the difference between the control run and the mean of the 50-member ensemble runs in 1998. The dots in (c) represent area statistically significant above 90% confidence level based on the Student's *t* test. The "Obs98" means the observed circulation in 1998, while the "Obs_clim" indicates the climatological mean between 1993 and 2022; the "CTRL98" means the circulation of 1998 in "CTRL" run, while the "CTRL_clim" represents the climatological mean of winds and vorticity from 1993 to 2022 in "CTRL" simulations; the "ENS" means the 50-member ensemble mean simulations.

(5 TCs), indicating an improved simulation accuracy by the large ensemble average, albeit still underestimating the actual TCGF of about −1.5 STDs as in observations.

Figure 3 displays the spatial distributions of the observed and simulated TCGF anomalies in 1998. Due to the strong impact of the decaying El Niño event, the observed TCGF shows a dominant negative anomaly over most of the WNP centered at 15°N, 140°E and a marginal increase in the coastal region of East Asia (Fig. 3a), giving rise to an unusually negative anomaly in the entire basin (Fig. 2b). Although the control run also simulated a dipole pattern similar to that in observation, the negative anomaly is much weaker and covers a narrower area than that in observation (Fig. 3b). This resulted in a negligible net change in the simulated TCGF in the basin in 1998. The large ensemble mean of TCGF anomalies in 1998 (relative to the climatological mean in the control run) also exhibits a dipole pattern similar to that in observation, but the negative TCGF anomaly mainly appears in a zonal-elongated region south of 20°E over the WNP, and the positive anomaly along the coastal region offshore of East Asia is considerably weaker than that in observation (Fig. 3c), resulting in an overall negative TCGF anomaly (blue bar in Fig. 2b). Figure 3d shows the TCGF difference between the control run in 1998 and the large ensemble mean in 1998. Clearly, the simulation bias largely originated from positive TCGF anomalies west of 150°E, including the coastal regions offshore of East Asia, and negative TCGF anomalies east of 150°E (Fig. 3d). In general, compared to the control run, the large ensemble mean provides a more robust and reliable representation of the simulated climate state and variability for the 1998 season and thus is chosen to examine the uncertainty among the ensemble runs.

4. Atmospheric modes responsible for the uncertainty

We compared the circulation anomalies in the simulation and the reanalysis (Fig. 4). In the reanalysis, easterly wind anomalies appear in the entire tropics, stretching from the date line to the SCS accompanied by a low-level anomalous anticyclonic circulation south of 30°N in the extratropics. Moreover, a dual-core negative vorticity anomaly is evident, with one centered over the SCS and the other centered over the east of the Philippines (Fig. 4a). This pattern is linked to the tremendous decrease in TCGF in 1998 (Fig. 3a). The control run for 1998 also captured the easterly anomalies extending from the date line to the Philippines but with a discrepancy in the form of a cyclonic circulation bias over the northern SCS (Fig. 4b)

Unauthenticated | Downloaded 11/13/26 12:23 PM UTC

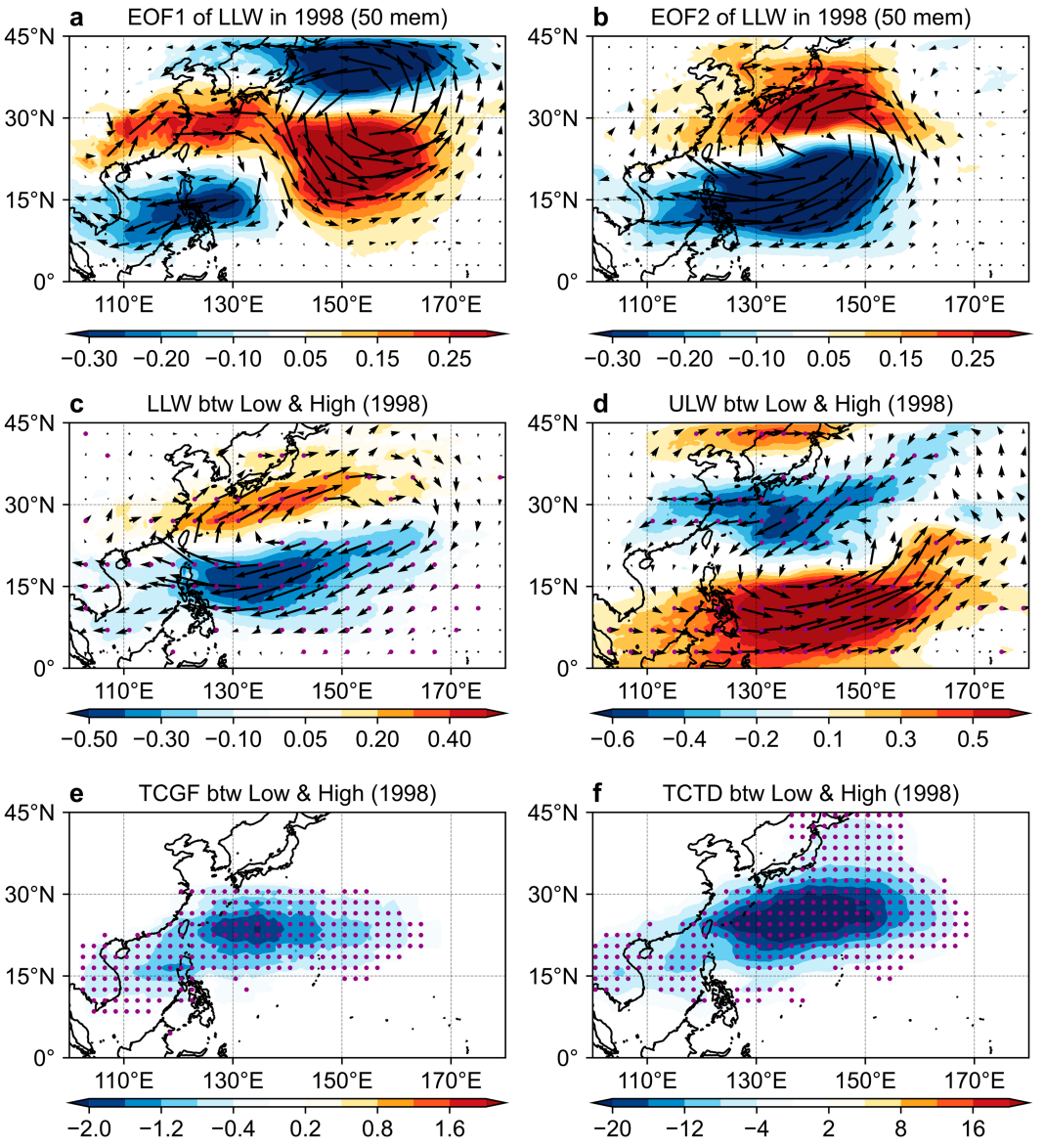


FIG. 5. The EOF analysis of LLWs and composite of winds, TCGF, and TCTD. (a) The EOF1 mode of LLWs across 50 members, (b) the EOF2 mode, (c) composite LLWs between low and high TCGF groups with each group containing 10 members, (d) composite upper-level winds, (e) composite difference in TCGF between low and high groups, and (f) composite difference in TCTF. The purple dots in (c)–(f) represent areas statistically significant above the 90% confidence level based on the Student's *t* test. The shadings in (a)–(d) stand for the zonal wind anomalies while for TCGF/TCTD in (e) and (f). The explained variance of EOF1 is 30.98% and that of EOF2 is 25.4%.

compared to the reanalysis (Fig. 4a). Consequently, this induces a positive bias in TCGF anomaly over the northern SCS in the control run (Fig. 3b). In addition, the simulated extratropical anticyclonic anomaly (15°–30°N, 120°–160°E) in the control run shows an eastward shift and a weaker magnitude than in the reanalysis (Fig. 4b), leading to the limited decrease in TCGF east of 130°E (Fig. 3b). The low-level circulation anomaly in the large ensemble mean relative to the climatology in the control run shows a pattern very similar to that in the reanalysis (Fig. 4c), indicating a reduction of simulation bias in low-level circulation anomaly than in the control run. The differences between the control run and the large ensemble mean in 1998 are characterized by a cyclonic circulation bias over the SCS and an anticyclonic circulation anomaly centered at around (140°E, 30°N) southeast of Japan (Fig. 4d), leading to a positive TCGF anomaly in the coastal region offshore of East Asia and a negative anomaly in southeast of Japan in the control run (Fig. 3d). Note that the large ensemble mean shows an overall improvement in reproducing the low-level circulation anomaly in 1998 compared with the control run (Figs. 4c,b).

Interestingly, the simulation bias in circulation patterns predominantly arises over the SCS and southeast of Japan

Unauthenticated | Downloaded 11/13/26 12:23 PM UTC

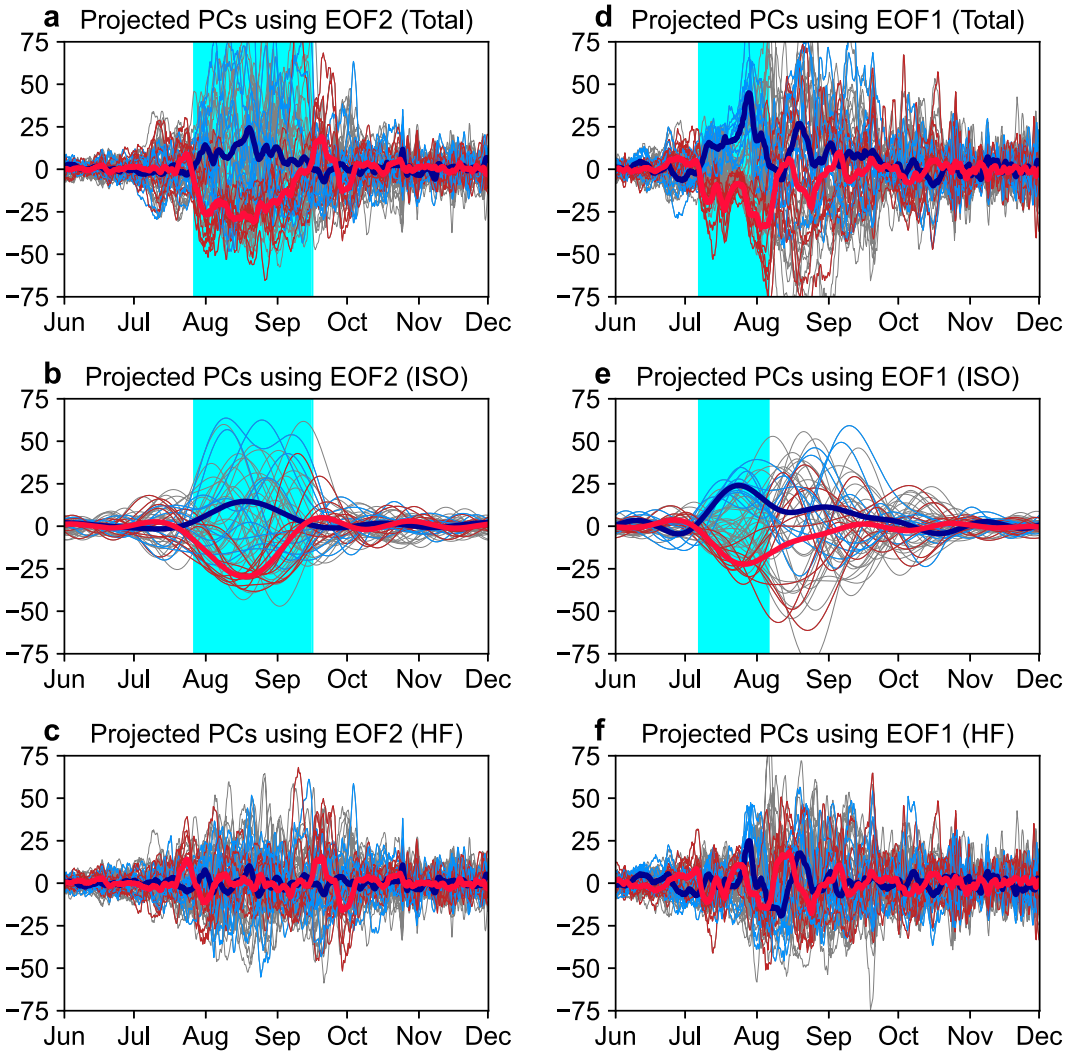


FIG. 6. Projected time series based on spatial patterns of EOFs in 1998. The spatial patterns of (a) EOF2 as shown in Fig. 2b and (d) EOF1 as shown in Fig. 2a, (b),(e) intraseasonal, and (c),(f) HF components based on (b),(c) EOF2 and (e),(f) EOF1. The shades in (a) and (b) represent the period from 25 Jul to 13 Sep 1998 with large variabilities. The blue (red) lines in (a)–(c) represent 10 members in the high (low) group. The thickest blue (red) lines in (d)–(f) represent the mean of 10 high (low) ensemble runs. Considering (left) EOF2, the runs for (right) EOF1 have been regrouped. The bold yellow (magenta) line is the average of the 10 ensemble runs in high group with positive (10 ensemble runs in low group with negative) values during the period from 10 Jul to 10 Aug.

(Fig. 4d). These patterns bear a resemblance to the known atmospheric dynamic modes, such as the monsoon trough (Lander 1996; Fig. 4d) or Matsuno–Gill (Gill 1980; Showman and Polvani 2010) mode over the SCS and Pacific–Japan pattern (Nitta 1989; Huang and Li 1989) extending from the SCS to southeast of Japan. Figures 5a and 5b show the EOF analysis of low-level winds (see method in section 2d). The first EOF (EOF1; Fig. 5a) is characterized by a dipole pattern of circulation anomalies, with an anticyclonic circulation anomaly extending from the SCS to west of 135°E and a cyclonic circulation anomaly in southeast of Japan. This mode closely resembles the circulation difference between the control run and the large ensemble mean in 1998 (Fig. 4d). The second EOF (EOF2) mode is identified by a basin-uniform anticyclonic circulation anomaly (Fig. 5b). For clarity, we will refer to EOF1 as the "dipole mode" and refer EOF2 as the "monopole mode." The monopole mode oscillating on intraseasonal time scale could contribute to intensification or weakening of the monsoon trough (Huangfu et al. 2017; Hu et al. 2019; Wang et al. 2021), correspondingly modulating the TC genesis east of the Philippines. The dipole mode indicates a southwestern–northeastern propagation pattern on intraseasonal time scale. It is very interesting to note that the simulation uncertainty across 50 ensemble members mainly originated from these two atmospheric dynamic modes (Figs. 5a,b).

To further investigate how the atmospheric dynamic modes affect circulation anomalies and the resulting uncertainty in simulating TCGF, we examined the anomalies of upper- and

Unauthenticated | Downloaded 11/13/26 12:23 PM UTC

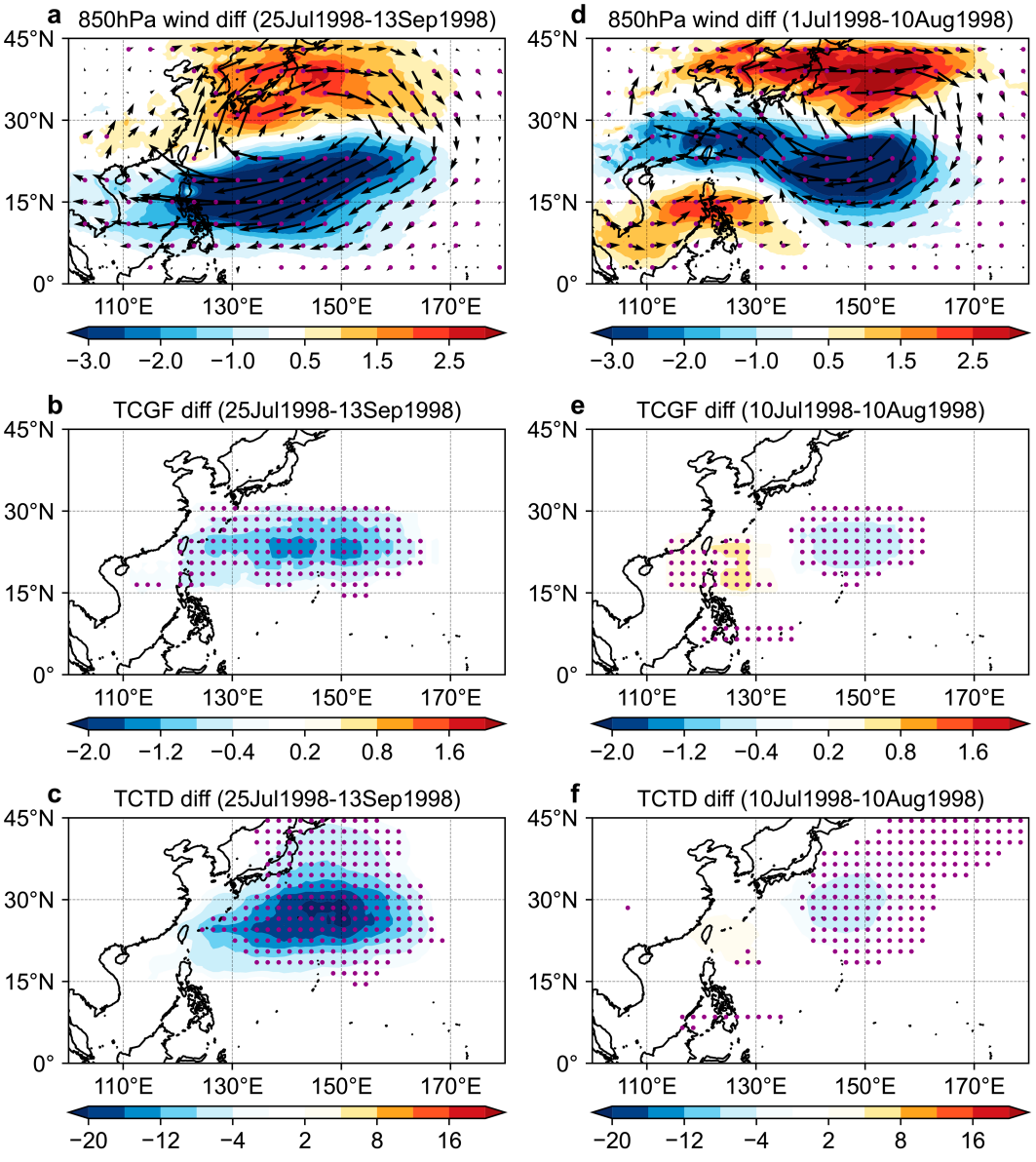


FIG. 7. Composite differences in (a),(d) LLW, (b),(e) TCGF, and (c),(f) TCTD anomalies between low and high groups between (left) 25 Jul and 13 Sep 1998 and the period from (right) 10 Jul to 10 Aug 1998. The purple dots represent areas statistically significant above the 90% confidence level based on the Student's *t* test.

low-level circulations, TCGF, and TC track density (TCTD) between the two groups of ensemble members (Figs. 5c–f). Two groups were categorized based on distinct TCGFs during the JJASON period. The high group consists of the 10 members with the highest TC frequency during JJASON, and the low group includes the 10 members with the lowest TC frequency during JJASON among the 50 large ensemble runs. The low-level wind anomaly between the composites of the low and high groups shows an anomalous anticyclonic circulation extending from the central SCS to the east of Japan, covering the main TC development region over the WNP (Fig. 5c). The upper-level wind anomaly is characterized by a cyclonic circulation anomaly south of 30°N and an anticyclonic circulation anomaly centered over Japan (Fig. 5d), also similar to the upper-tropospheric circulation of the typical Pacific–Japan pattern (Nitta 1989; Huang and Li 1989). In the simulations, the negative TCGF anomaly is mainly confined between 15° and 30°N, corresponding with the anomalous anticyclonic circulation anomaly (Fig. 5e), while the negative TCTD anomaly extends further northeastward (Fig. 5f).

5. Contribution of intraseasonal variability to uncertainty in the simulated TCGF

Since the subseasonal variability may play a critical role in modulating seasonal TC activity (Liu et al. 2021), we examine

Unauthenticated | Downloaded 11/13/26 12:23 PM UTC

TABLE 1. The occurrence counts of TCGF and TCTD for the high and low groups (each of 10-member average). Here, the composite of TCGF is for JJASON; the count of the monopole mode is from 25 Jul to 13 Sep 1998; and the count of the dipole mode is from 10 Jul to 10 Aug 1998. The differences between the low and high groups are shown in the brackets of low groups.

	Genesis_high	Genesis_low	Track_high	Track_low
Composite (JJASON)	15.2	7.5 (−7.7)	299.9	159.9 (−140)
Monopole mode (25 Jul–13 Sep)	7.7	2.9 (−4.8)	176.5	81.1 (−95.4)
Dipole mode (10 Jul–10 Aug)	2.3	1.9 (−0.4)	72.5	47.2 (−25.3)

and quantify the contributions of the identified two atmospheric dynamic modes on intraseasonal time scale to the uncertainty in the simulated TCGF/TCTD. We projected the 6-hourly low-level wind data onto the seasonal mean low-level wind pattern corresponding to EOF2 (Fig. 5b) to obtain the time series for the 50 members (Fig. 6a) as the method introduced in section 2. An interesting result is that the large spread (indicative of simulation uncertainty) of the large ensemble runs appears only from 25 July to 13 September 1998 (Fig. 6a). This indicates that the large differences in TCGF/TCTD between low and high groups in the large ensemble runs are primarily dictated by the anticyclonic circulation anomalies of the monopole mode during this period. More importantly, the intraseasonal variability contributes significantly to the simulation uncertainty (Fig. 6b), while the impact of high-frequency (HF) variability is very marginal (Fig. 6c). The average of the projected 6-hourly low-level wind anomalies from 25 July to 13 September 1998 between the low and high groups (Fig. 7a) clearly indicates the basin-uniform anticyclonic circulation anomaly on the intraseasonal time scale, consistent with the monopole mode on the seasonal time scale. The discrepancy in TCGF (TCTD) anomaly between the low and high groups during JJASON is quantified as −7.7 (−140) (Table 1; Figs. 5e,f). The JJASON-averaged TCGF/TCTD anomalies are largely determined by the difference (−4.8/−95.4) between 25 July and 13 September (Table 1; Figs. 7b,c vs Fig. 6b), accounting for 62.3%/68.1% of the corresponding total variance.

The above analyses suggest that the TCGF/TCTD differences (Figs. 7b,c) between the low and high groups are primarily governed by the intraseasonal anticyclonic and cyclonic circulation anomalies from the monopole mode (Figs. 6b and 7b,c). Although the dipole mode (Fig. 5a) also contributes to the simulation uncertainty (Fig. 4d), its contribution remains smaller than the monopole mode (Table 1). To clarify this, we examined large variabilities in the first PCs (Fig. 7d) from early July to early August 1998. To separate the dominant influence of the monopole mode from August to September, we sorted the time series of 50 members by averaging the PC1s from 10 July to 10 August 1998 to identify 10 high-TCGF and 10 low-TCGF members (Figs. 7d–f). We noticed that the projected PC1 also exhibits intraseasonal variability, albeit over a shorter period than the PC2. Furthermore, these projected PC1s have weaker impacts on TCGF over the entire WNP (Fig. 7e; a difference of 2.3 vs 1.9 TCs during this period). Instead, the related environmental conditions cause a redistribution of TC genesis locations among ensemble members (Figs. 7d,e), thus contributing to the simulation uncertainty. Although the dipole mode (Fig. 7d) contributes less to the WNP TCGF change, it significantly influences TCTD (Fig. 7f), with an average occurrence count of 72.5 for the high group compared to just 42.7 for the low group from 10 July to 10 August 1998.

As indicated above, the simulation uncertainty in TCGF is mainly associated with the monopole mode, which is closely related to the Pacific–Japan pattern, while the uncertainty in TC genesis location is predominantly influenced by the dipole mode (Figs. 5a and 7d). Previously, the monopole and dipole modes were perceived as two distinct and independent modes. A question naturally arises as to whether these two modes exist interconnectedly. To address this question, we examined the lead–lag regression of 850-hPa winds upon the respective PC1 and PC2 in 1998 with the results shown in Fig. 8. Notably, the simultaneous regression analysis demonstrates that the dipole and monopole modes correspond to different phases within the intraseasonal time scale (Figs. 8c,d). Further, we conducted an 11-day lead (8-day lag) regression upon PC1 (PC2), with the results shown in Fig. 8e (Fig. 8f). It is interesting to see that the dipole mode can evolve into a mode very similar to the monopole mode (Fig. 8e), while the monopole also can turn to a mode similar to the dipole mode (Fig. 8f).

To confirm the above results based on the singular year of 1998, we expanded our analysis to include the EOF analysis and lead–lag regression of the observed 850-hPa winds upon respective PC1 and PC2 for the JJASON season from 1993 to 2022 (Fig. 9). Two prominent features are revealed in Fig. 9. First, the observed low-level winds are predominantly influenced by the dipole mode (Fig. 9e) and the monopole mode (Fig. 9d), despite the changing order of these two EOF modes. Second, the observation clearly displays the evolution from the dipole mode to the monopole mode in both EOF1 (Figs. 9a–d) and EOF2 (Figs. 9e–h). For EOF1, the low-level winds show a dipole pattern at −9d, with an anticyclonic anomaly north of 30°N and a cyclonic anomaly from the SCS to the WNP south of 30°N (Fig. 9a). Subsequently, the anomalous cyclone in the south gradually intensified and expanded northward, while the anomalous anticyclone in the north gradually weakened and dissipated, ultimately evolving into a monopole mode at 0d (Fig. 9d). Similarly, for EOF2, the anomalous anticyclone in the north gradually weakened and dissipated, ultimately evolving into a monopole mode at 10d (Fig. 9h). Note that PC1 and PC2 are mathematically orthogonal with a 90° phase difference or 1/4 of the period. Therefore, the regression from 9 to 10 days means the period between 36 (9 × 4) and 40 (10 × 4) days. These respond well to the propagation and development of intraseasonal variability. This highly suggests that these two modes are interactive and transformable. As the perturbation advances northeastward, it develops into a basin-scale cyclonic or anticyclonic circulation, leading to the Pacific–Japan

Unauthenticated | Downloaded 11/13/26 12:23 PM UTC

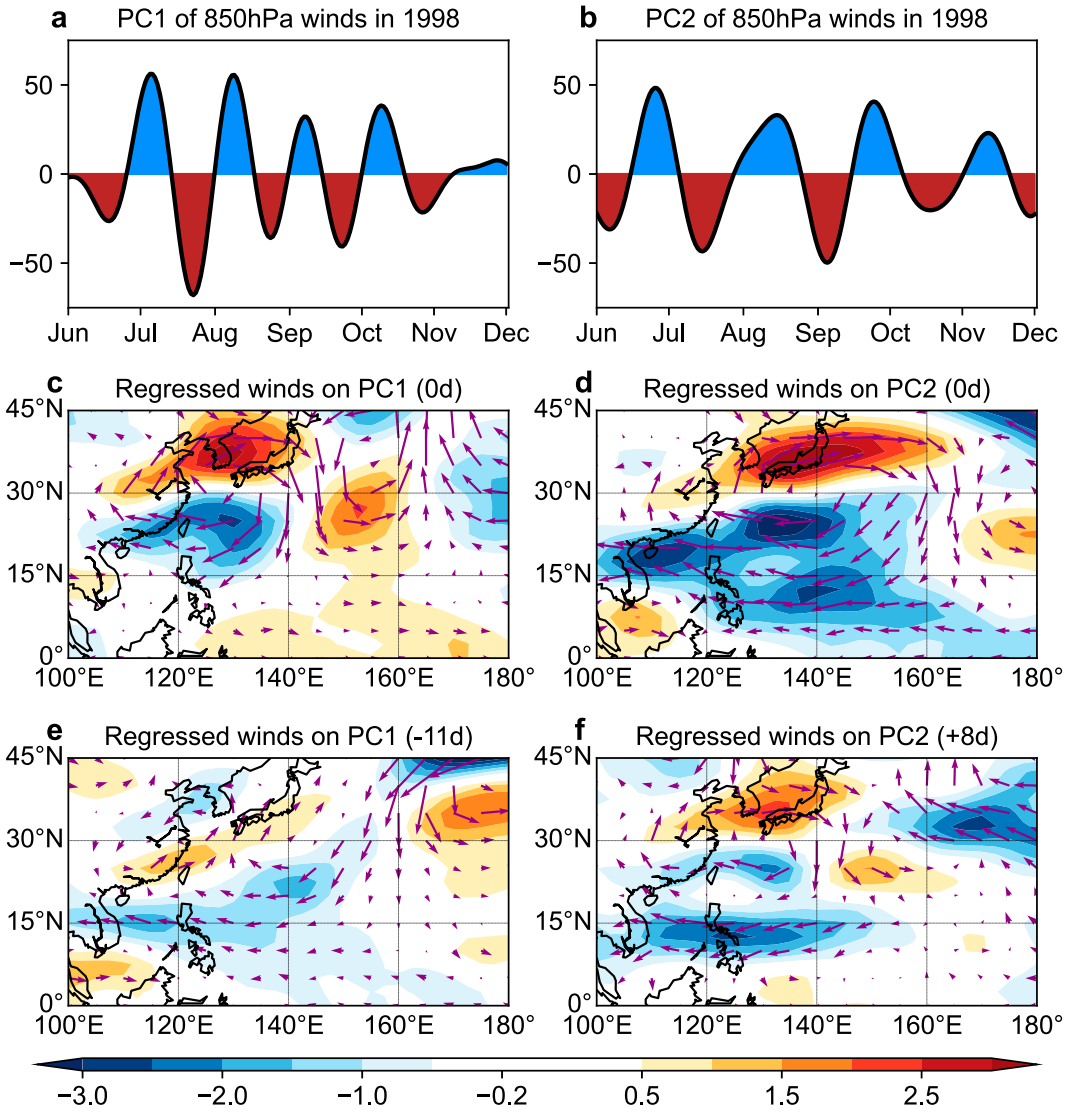


FIG. 8. Lead–lag regression of 20–90d-filtered 850-hPa winds upon respective (left) PC1 and (right) PC2 in 1998. (a) PC1, (b) PC2, simultaneous regression of LLW upon (c) PC1 and (d) PC2, (e) 11-day lead regression of 850-hPa wind anomalies upon PC1, and (f) 8-day lag regression of LLW upon PC2. The vectors represent regressed winds; meanwhile, the shades stand for the zonal component.

(monopole) mode (Figs. 7a and 8e). Interactively, the decaying Pacific–Japan mode southeast of Japan, coupled with the developing Matsuno–Gill mode over the SCS, evolves into the dipole mode as seen from the wind anomalies in Figs. 5a, 7d, and 8f. In general, the above results imply that the simulation uncertainty in TCGF is dominantly modulated by two intraseasonal atmospheric dynamic modes, which are also intrinsically interconnected.

Furthermore, we conducted a quantitative analysis to explore the relationship between intraseasonal variability uncertainty and TCGF uncertainty. Figures 10a and 10b show the relationship between TCGF and BSISO across 50 ensemble members. Here, the BSISO index was represented by the normalized PC2 (as shown in Fig. 6b), which is because the monopole mode (EOF2) controls TC genesis over the whole WNP. A positive value of BSISO indicates the anomalous anticyclone (inactive phase; Fig. 5b), indicating that it is negatively correlated with TCGF. As expected, a significant negative correlation exists between TCGF and BSISO intensity, with a correlation coefficient of −0.34 for JJASON and −0.54 averaged in the high-uncertainty period from 28 July to 13 September 1998. Both are significant at the 95% confidence level. That means that the stronger the simulated BSISO, the higher the simulated TCGF; conversely, the weaker the BSISO, the lower the TCGF. This strongly indicates that the uncertainty of BSISO in the simulation would greatly affect the reliability of TCGF simulations. Consequently, TCGF simulations could be improved by constraining BSISO intensity. To test this, we selected the 10 ensemble members with the most inactive BSISO simulations in the

Unauthenticated | Downloaded 11/13/26 12:23 PM UTC

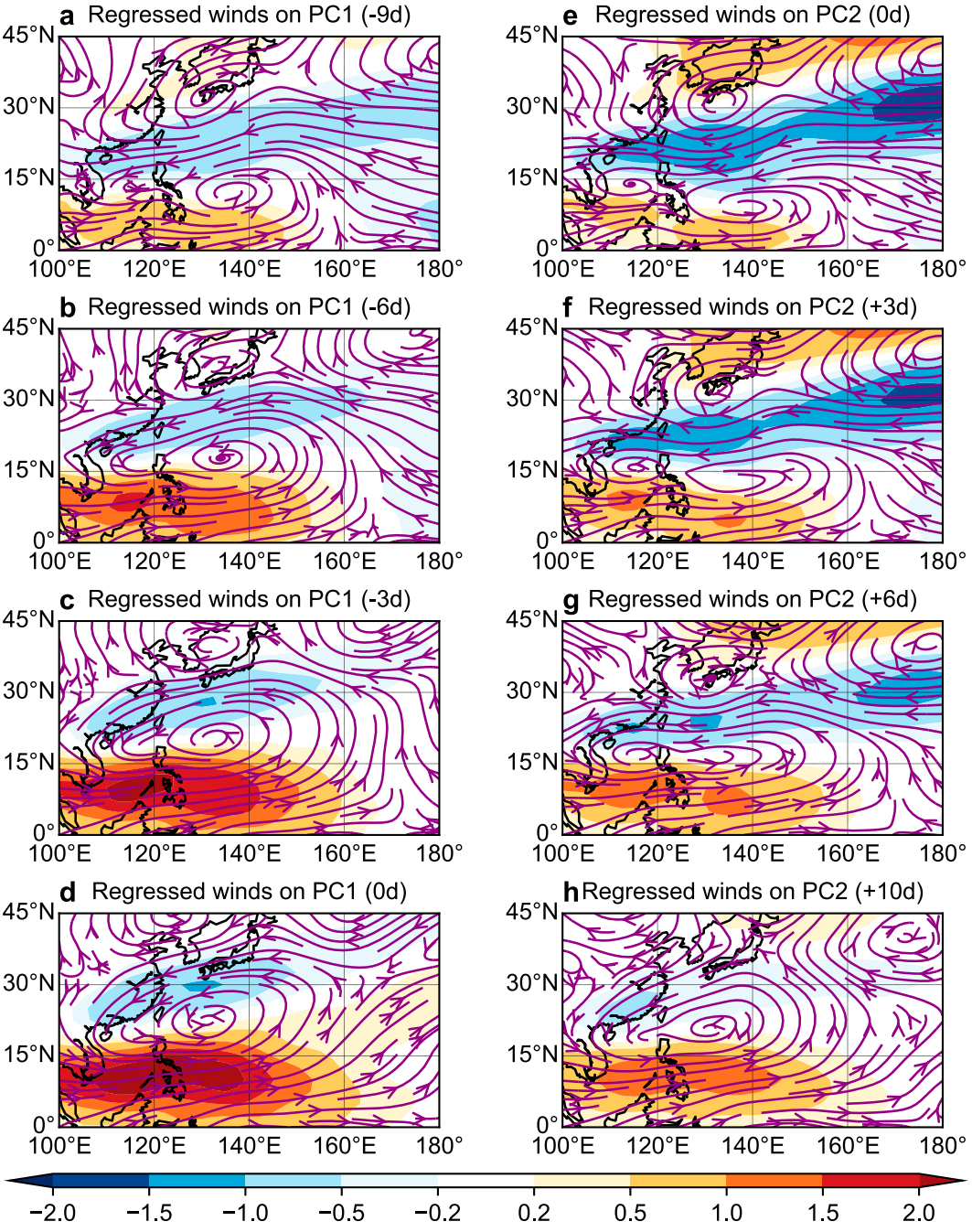


FIG. 9. Lead–lag regression of the observed 850-hPa winds (streamlines) upon respective (left) PC1 and (right) PC2 for the JJASON season from 1993 to 2022. (a)–(d) The leading regression of 850-hPa winds upon PC1; (e),(f) the lag regression of 850-hPa winds upon PC2. Here, the simultaneous regression upon PC1 is revealed in (d), and the simultaneous regression upon PC2 is shown in (e). The shading represents the zonal wind anomalies.

high-uncertainty period, which closely matched the observed BSISO intensity, and the 10 ensemble members with the most active ISO simulations (Fig. 10c). The former resulted in TCGF simulations that were closer to observations compared to the ensemble mean. Conversely, the latter led to greater deviation from observed TCGF. This analysis demonstrates that ISO uncertainty is indeed a key contributor to TCGF uncertainty and provides a practical pathway for enhancing model simulations.

6. Discussion

As indicated in section 2b, this study only focused on a single year of 1998 due to the immense computational demands.

Unauthenticated | Downloaded 11/13/26 12:23 PM UTC

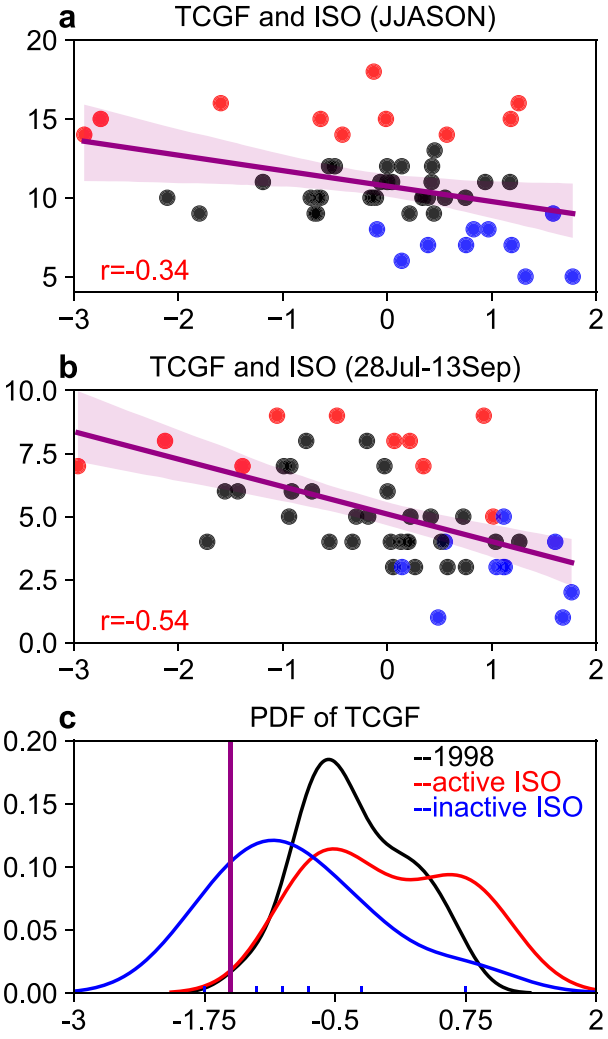


FIG. 10. Scatterplots illustrating the relationship between TCGF and BSISO (represented by PC2), accompanied by the probability density function (PDF) of TCGF under various BSISO phase constraints. (a) Scatterplot of TCGF (ordinate) against the BSISO index (abscissa), represented by the normalized season-averaged PC2 (referenced from Fig. 6b). (b) As in (a), but both TCGF and BSISO are calculated during the high-uncertainty period from 28 Jul to 13 Sep 1998. (c) PDF distribution of TCGF across all 50 ensemble members (black), with active (red) and inactive (blue) BSISO phases highlighted for the 10 selected members during the same period. In (a) and (b), red dots represent the 10 members with the highest TCGF, while blue dots indicate the 10 members with the lowest. The purple line represents the regression line, with a shaded 95% confidence interval based on bootstrap testing. The correlation coefficients between TCGF and BSISO are shown in (a) and (b). In (c), the horizontal axis represents the STD from the climatological mean TCGF, and the purple line denotes the observed TCGF.

To further confirm the above results, we conducted an additional analysis for the year 2009, which was an El Niño year. Unlike 1998, the simulation for 2009 exhibited minimal bias (Fig. 2c). Notably, intraseasonal variability in 2009 showed diverse behaviors during JJASON (Fig. 11). The difference in annual TC count between the high and low groups was 2.1, accounting for about 25.9% of the total difference of 8.1 during JJASON. This percent is much lower than that in 1998.

It is well known that the daily OLR data can be used as a proxy for tropical convection. Here, simulation uncertainty on the intraseasonal time scale was represented by the spread in filtered OLR across 50 ensemble members. Figure 12 demonstrates the evolution of simulation uncertainty represented by the 20–90d-filtered OLR spread across 50 ensemble members in 1998. For comparison, similar results in 2009 are also presented in Fig. 11. Note that we have repeated all analyses for 2009 and got similar results to those for 1998, but considering the fact that the OLR analysis sufficiently demonstrates the key differences in ISO between the 2 years; here, we only included the OLR analysis in 2009. A prominent feature is that the simulation uncertainty represented by the OLR spread originates from the southern SCS and east of the Philippines. It remains weak before mid-July but grows slowly and extends northeastward. The uncertainty reaches its peak in August, after which it weakens. Another interesting feature is that the magnitude of simulation uncertainty in 2009 is about half of that in 1998 during August–September. This indicates that the intraseasonal variability plays an important role in causing the uncertainty in seasonal simulations of TCGF. When intraseasonal variability exhibits high uncertainty, the resulting uncertainty in TCGF simulation will also be large, and vice versa.

Another interesting question arises as to the source of uncertainty in intraseasonal variability. At the present, there is insufficient evidence that can reasonably explain it. However, there are some clues that may shed light on this issue. As indicated above, 1998 was a La Niña year, while 2009 was an El Niño year. Previous studies have pointed out that BSISO activity over the western Pacific is significantly weakened (strengthened) in La Niña (El Niño) developing summer (Tang and Yu 2008; Chen et al. 2016; Kikuchi 2021; Lee et al. 2022). Further studies have also estimated the predictability of BSISO (Lee et al. 2015; Wang et al. 2019). They revealed that the predictability depends on the model and strength of the BSISO events, with stronger events generally exhibiting greater predictability. Since 1998, a La Niña year, featured a weaker BSISO event, it could contribute to the larger simulation uncertainty in BSISO activity as shown in Fig. 12, thus leading to the largest uncertainty in TCGF simulation. An opposite situation corresponds to 2009, with a stronger BSISO event and low uncertainty in TCGF simulation. To further confirm this result, we explore the relationship between ENSO and the simulation bias of TCGF (Fig. 2c). We define El Niño years and La Niña years based on the JJASON-averaged Niño-3.4 index above 0.8 standard deviation and below −0.8 standard deviation, respectively. As a consequence, 5 El Niño years (1993, 1997, 2002, 2009, 2015) and 10 La Niña years (1995, 1998, 1999, 2007, 2008, 2010, 2016, 2017, 2020, and 2021) are identified. As expected, among the 5 El Niño years, the simulation bias of TCGF was smaller than the average for 1993–2022 in all cases, with a perfect compliance rate of 100%. Notably, the El Niño years of 1997, 2009, and 2015 ranked as the top 3 years with the smallest biases during 1993–2022. In contrast, among the 10 La Niña years, except for years 2007 and 2017, the simulation bias of TCGF

Unauthenticated | Downloaded 11/13/26 12:23 PM UTC

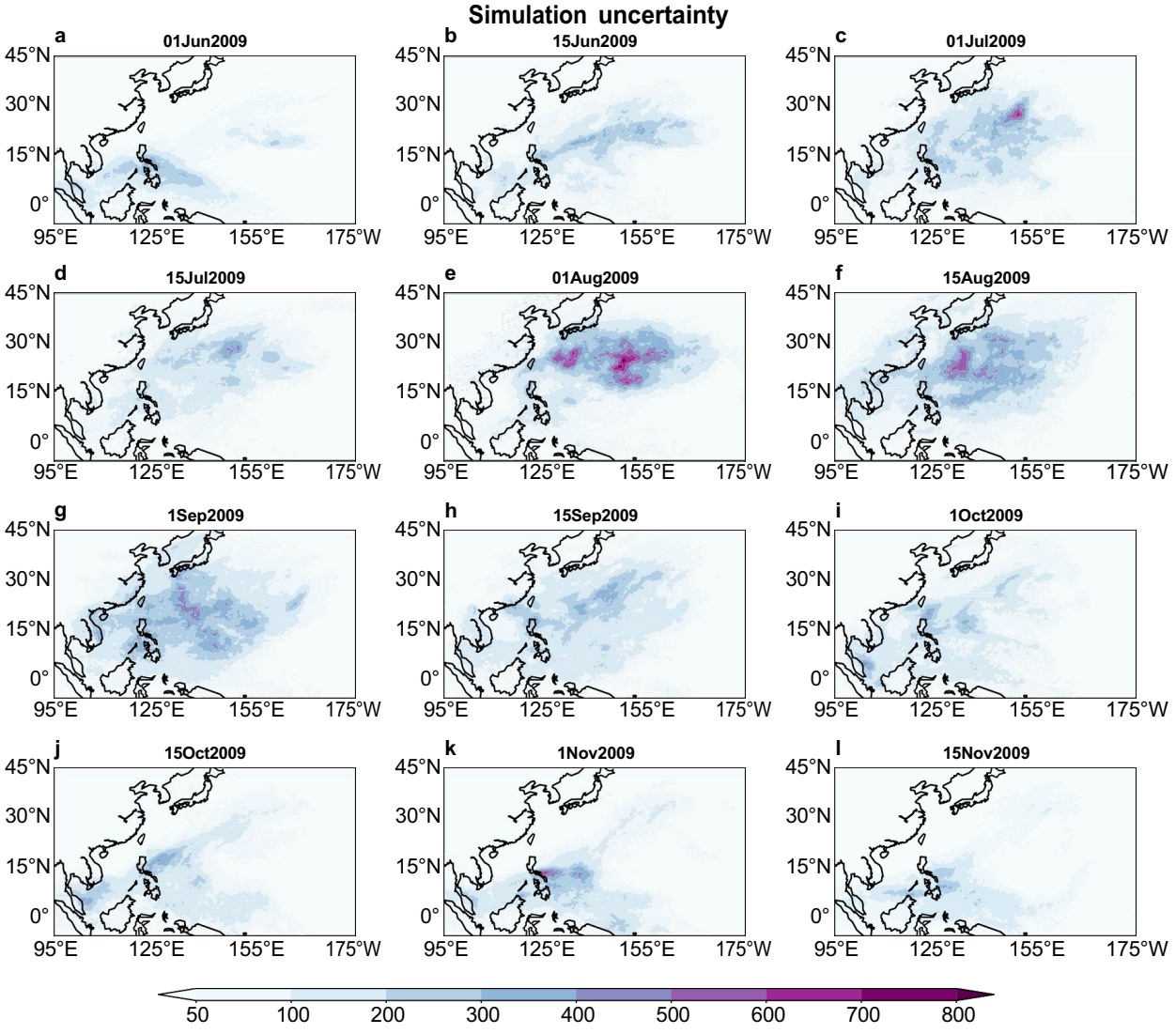


FIG. 11. The evolution of simulation uncertainty represented by the intraseasonal OLR spread across 50 ensemble members in 2009. (a)–(l) The daily evolution from 1 Jun 2009 to 15 Nov 2009.

in the remaining 8 years is above normal, with a compliance rate of 80%.

To further confirm the above discussion, we have analyzed the observed mean ISO variance averaged in the tropical western Pacific (5°S–10°N, 100°E–180°) and the simulated bias in TCGF in the typhoon season from 1993 to 2022, with the results shown in Fig. 13. Here, the ISO variance is calculated based on the zonal and meridional winds bandpass filtered between 20 and 60 days. We can see that the simulated biases in TCGF are negatively correlated with the ISO variances during 1993–2022, with the correlation coefficient reaching −0.58, which is statistically significant above the 95% confidence level. Especially, the years 1997 and 2015, which were both super El Niño years, correspond to peak ISO variance values. This further confirms that the ISO significantly affects the predictability of TCGF. Namely, strong ISO greatly suppresses the uncertainty in the simulated TCGF, and vice versa. This is consistent with the results for 1998 and 2009 as demonstrated with 50 ensemble simulations for each of the years.

These results underscore the source of uncertainty in intraseasonal variability to a large extent in the simulation bias of TCGF. Or alternatively, the large intraseasonal variability can enhance the predictability of TCGF over the WNP. Nevertheless, further studies to understand how intraseasonal variability contributes to uncertainty in simulating seasonal TC activity would be helpful in reducing the model biases and improving seasonal prediction of TC activity.

7. Conclusions

This study examined uncertainty in the seasonal simulations of TCGF over the WNP based on 50-member ensemble

Unauthenticated | Downloaded 11/13/26 12:23 PM UTC

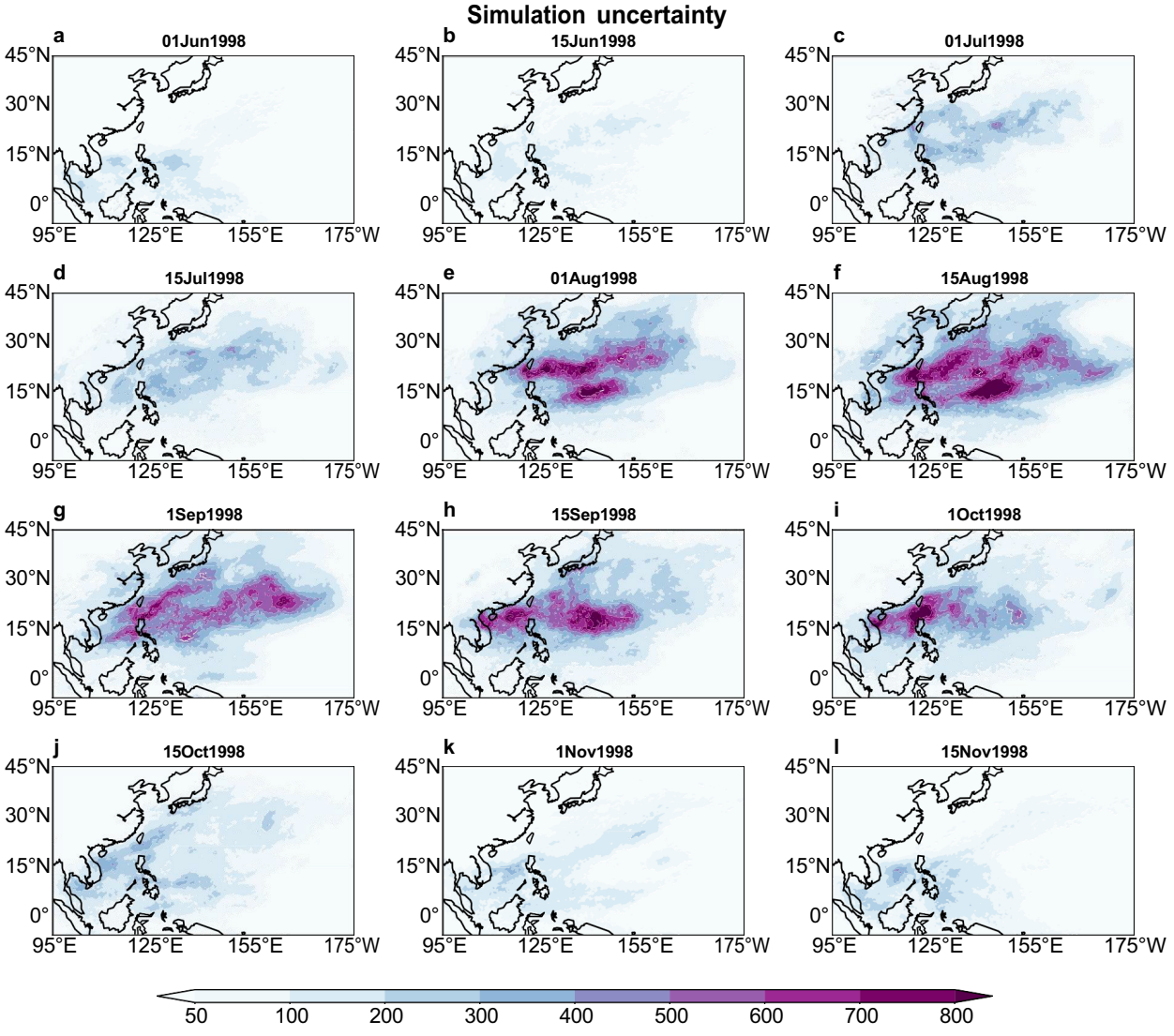


FIG. 12. The evolution of simulation uncertainty represented by the intraseasonal OLR spread across 50 ensemble members in 1998. (a)–(l) The daily evolution from 1 Jun 1998 to 15 Nov 1998.

simulations in 1998 using the high-resolution RegCM. The year 1998 witnessed the unusually few TCs forming over the WNP with a deviation of −1.5 STDs during 1993–2022. The simulated TCGF in 1998 exhibited the largest uncertainty among 1993–2022, spanning from +1 to −1.75 STDs. This simulation uncertainty was found to stem from two intrinsic atmospheric dynamic modes: the monopole and dipole modes. Further analysis revealed that these two modes were dominated by intraseasonal variabilities mainly concentrated in July–September. The monopole mode significantly affects the TCGF/TCTD from the end of July to early September, accounting for approximately 62.3% of the simulation uncertainty throughout the entire TC season (JJASON). The dipole mode plays an important role in shifting the TC genesis locations on subseasonal time scales. The two intraseasonal modes can further feedback to the seasonal mean state, leading to considerable bias and large uncertainty in the simulated TCGF/TCTD. Moreover, it is found that the two modes are intrinsically interconnected on intraseasonal time scale, allowing the dipole mode to evolve into the monopole mode through northeastward propagation and vice versa. By conditionally constraining BSISO intensity, we can significantly reduce model uncertainty in simulating TCGF. In addition, results from large ensemble simulations for 2009 confirm the findings for 1998. The uncertainty in 2009 is considerably lower than that in 1998, which is consistent with the large intraseasonal variability in 2009, a year with developing El Niño. In contrast, 1998 was a La Niña year with relatively weak intraseasonal variability. This also implies that large intraseasonal variability can be source of predictability of seasonal TC activity.

While this study has made strides in understanding the role of intraseasonal variability in contributing to the simulation uncertainty of TCGF over the WNP, several limitations and avenues for future research emerge from our findings. First, recognizing the possible impact of varying thresholds on TC detection, we

Unauthenticated | Downloaded 11/13/26 12:23 PM UTC

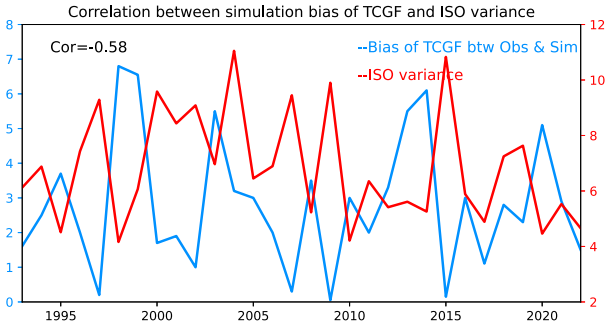


FIG. 13. The observed mean ISO variance averaged over the tropical western Pacific (5°S–10°N, 100°E–180°) and the simulated bias in TCGF in the typhoon season during 1993–2022. Here, the ISO variance is calculated based on the zonal and meridional winds bandpass filtered between 20 and 60 days. The correlation coefficient (Cor) reaches −0.58, which is statistically significant above the 95% confidence level.

examined the vortex lifespan from 2 days to 1 day and found that the TCGF calculated based on the 2-day threshold and that observed bear a higher correlation, with the coefficient above 0.75. Despite the increased linear trend of TCGF from 1993 to 2022 and climatological TC count with the lower threshold for lifespan, the main conclusions remained consistent, indicating the dominant role of the monopole and dipole modes in controlling TC activity over the WNP, as well as in inducing simulation uncertainty. Second, our results are based on a regional climate model in this study while it is worthy of comparing with global climate models to quantify the relative importance of local or remote forcings to the simulation uncertainty. Third, the intraseasonal variability is often connected to larger-scale climate phenomena, such as ENSO (Liu et al. 2018; Li et al. 2020), which was not explored in this study.

Since the sources of uncertainties identified in this study are physical modes, the findings here should be applicable to other global/regional climate models. For instance, the dipole mode and monopole mode resemble the "Pacific–Japan" mode and the "Matsuno–Gill" mode found in our previous study based on 100 ensemble runs using Japan MRI model (Zhao et al. 2023a). However, we focused on the seasonal mean (June–November averaged) in Zhao et al. (2023a), but here, we applied the analysis to intraseasonal variability. Therefore, the findings should not be generic for the particular model we used in this study. Future work could benefit from a more detailed examination of how these and other climate patterns may interact and modulate the monopole and dipole modes, potentially offering a holistic view of mechanisms driving TC activity and predictability.

Acknowledgments. This work is supported by the National Nature Science Foundation of China (Grants 42288101, 42105022, and 42075015), the Guidance Project for Industrial Technology Development and Application Plan of Fujian Province (NO.2024Y0075), and the Academician Workstation of AP-TCRC.

Data availability statement. In this study, the TC information data were downloaded from IBTrACS, version 4 (https://www.ncei.noaa.gov/products/international-best-track-archive); the NCEP reanalysis data are obtained from https://downloads.psl.noaa.gov/Datasets/ncep.reanalysis.derived/pressure/); and the SST data are derived from https://www.metoffice.gov.uk/hadobs/hadisst/data/download.html.

REFERENCES

Ahn, M.-S., and Coauthors, 2020: MJO propagation across the maritime continent: Are CMIP6 models better than CMIP5 models? *Geophys. Res. Lett.*, **47**, e2020GL087250, https://doi.org/10.1029/2020GL087250.

Camargo, S. J., and A. A. Wing, 2016: Tropical cyclones in climate models. *Wiley Interdiscip. Rev.: Climate Change*, **7**, 211–237, https://doi.org/10.1002/wcc.373.

——, and Coauthors, 2019: Tropical cyclone prediction on subseasonal time-scales. *Trop. Cyclone Res. Rev.*, **8**, 150–165, https://doi.org/10.1016/j.tcrr.2019.10.004.

Chen, X., J. Ling, and C. Li, 2016: Evolution of the Madden–Julian oscillation in two types of El Niño. *J. Climate*, **29**, 1919–1934, https://doi.org/10.1175/JCLI-D-15-0486.1.

Chen, Z., T. Zhou, X. Chen, W. Zhang, L. Zhang, M. Wu, and L. Zou, 2022: Observationally constrained projection of Afro-Asian monsoon precipitation. *Nat. Commun.*, **13**, 2552, https://doi.org/10.1038/s41467-022-30106-z.

Emanuel, K., 2010: Tropical cyclone activity downscaled from NOAA-CIRES reanalysis, 1908–1958. *J. Adv. Model. Earth Syst.*, **2**, 1, https://doi.org/10.3894/JAMES.2010.2.1.

Feng, X., R. Toumi, M. Roberts, K. I. Hodges, and P. L. Vidale, 2023: An approach to link climate model tropical cyclogenesis bias to large-scale wind circulation modes. *Geophys. Res. Lett.*, **50**, e2023GL103838, https://doi.org/10.1029/2023GL103838.

Fu, X., and P.-C. Hsu, 2011: Extended-range ensemble forecasting of tropical cyclogenesis in the northern Indian Ocean: Modulation of Madden-Julian oscillation. *Geophys. Res. Lett.*, **38**, L15803, https://doi.org/10.1029/2011GL048249.

——, J.-Y. Lee, P.-C. Hsu, H. Taniguchi, B. Wang, W. Wang, and S. Weaver, 2013: Multi-model MJO forecasting during DYNAMO/CINDY period. *Climate Dyn.*, **41**, 1067–1081, https://doi.org/10.1007/s00382-013-1859-9.

Gill, A. E., 1980: Some simple solutions for heat-induced tropical circulation. *Quart. J. Roy. Meteor. Soc.*, **106**, 447–462, https://doi.org/10.1002/qj.49710644905.

Ham, Y.-G., and J.-S. Kug, 2015: Role of north tropical Atlantic SST on the ENSO simulated using CMIP3 and CMIP5 models. *Climate Dyn.*, **45**, 3103–3117, https://doi.org/10.1007/s00382-015-2527-z.

Henley, B. J., J. Gergis, D. J. Karoly, S. Power, J. Kennedy, and C. K. Folland, 2015: A tripole index for the interdecadal Pacific oscillation. *Climate Dyn.*, **45**, 3077–3090, https://doi.org/10.1007/s00382-015-2525-1.

Hsu, P.-C., Y. Qian, Y. Liu, H. Murakami, and Y. Gao, 2020: Role of abnormally enhanced MJO over the western Pacific in the formation and subseasonal predictability of the record-breaking northeast Asian heatwave in the summer of 2018. *J. Climate*, **33**, 3333–3349, https://doi.org/10.1175/JCLI-D-19-0337.1.

Hu, K., G. Huang, S.-P. Xie, and S.-M. Long, 2019: Effect of the mean flow on the anomalous anticyclone over the indo-northwest Pacific in post-El Niño summers. *Climate Dyn.*, **53**, 5725–5741, https://doi.org/10.1007/s00382-019-04893-z.

Huang, B., and Coauthors, 2017: Extended Reconstructed Sea Surface Temperature, version 5 (ERSSTv5): Upgrades, validations,

Unauthenticated | Downloaded 11/13/26 12:23 PM UTC

and intercomparisons. *J. Climate*, **30**, 8179–8205, https://doi.org/10.1175/JCLI-D-16-0836.1.

——, C. Liu, V. Banzon, E. Freeman, G. Graham, B. Hankins, T. Smith, and H.-M. Zhang, 2021: Improvements of the Daily Optimum Interpolation Sea Surface Temperature (DOISST) version 2.1. *J. Climate*, **34**, 2923–2939, https://doi.org/10.1175/JCLI-D-20-0166.1.

Huang, R., and L. Li, 1989: Numerical simulation of the relationship between the anomaly of subtropical high over East Asia and the convective activities in the western tropical Pacific. *Adv. Atmos. Sci.*, **6**, 202–214, https://doi.org/10.1007/BF02658016.

Huang, X., and Coauthors, 2020: South Asian summer monsoon projections constrained by the interdecadal Pacific oscillation. *Sci. Adv.*, **6**, eaay6546, https://doi.org/10.1126/sciadv.aay6546.

——, T. Zhou, J. C. L. Chan, R. Zhan, Z. Chen, and J. Zhao, 2023: Understanding uncertainties in projections of western North Pacific tropical cyclogenesis. *Environ. Res. Lett.*, **18**, 114037, https://doi.org/10.1088/1748-9326/ad02ad.

Huangfu, J., R. Huang, W. Chen, T. Feng, and L. Wu, 2017: Interdecadal variation of tropical cyclone genesis and its relationship to the monsoon trough over the western North Pacific. *Int. J. Climatol.*, **37**, 3587–3596, https://doi.org/10.1002/joc.4939.

Jiang, X., M. Zhao, E. D. Maloney, and D. E. Waliser, 2016: Convective moisture adjustment time scale as a key factor in regulating model amplitude of the Madden-Julian oscillation. *Geophys. Res. Lett.*, **43**, 10412–10419, https://doi.org/10.1002/2016GL070898.

Jin, F.-F., 1997: An equatorial ocean recharge paradigm for ENSO. Part I: Conceptual model. *J. Atmos. Sci.*, **54**, 811–829, https://doi.org/10.1175/1520-0469(1997)054<0811:AEORPF>2.0.CO;2.

Kalnay, E., and Coauthors, 1996: The NCEP/NCAR 40-Year Reanalysis Project. *Bull. Amer. Meteor. Soc.*, **77**, 437–471, https://doi.org/10.1175/1520-0477(1996)077<0437:TNYRP>2.0.CO;2.

Kikuchi, K., 2021: The Boreal Summer Intraseasonal Oscillation (BSISO): A review. *J. Meteor. Soc. Japan*, **99**, 933–972, https://doi.org/10.2151/jmsj.2021-045.

Knapp, K. R., M. C. Kruk, D. H. Levinson, H. J. Diamond, and C. J. Neumann, 2010: The International Best Track Archive for Climate Stewardship (IBTrACS): Unifying tropical cyclone data. *Bull. Amer. Meteor. Soc.*, **91**, 363–376, https://doi.org/10.1175/2009BAMS2755.1.

——, H. J. Diamond, J. P. Kossin, M. C. Kruk, and C. J. Schreck, 2018: International Best Track Archive for Climate Stewardship (IBTrACS) project, version 4. NOAA National Centers for Environmental Information, accessed 10 January 2023, https://doi.org/10.25921/82TY-9E16.

Knutson, T. R., J. J. Sirutis, S. T. Garner, G. A. Vecchi, and I. M. Held, 2008: Simulated reduction in Atlantic hurricane frequency under twenty-first-century warming conditions. *Nat. Geosci.*, **1**, 359–364, https://doi.org/10.1038/ngeo202.

Knutson, T., and Coauthors, 2019: Tropical cyclones and climate change assessment: Part I: Detection and attribution. *Bull. Amer. Meteor. Soc.*, **100**, 1987–2007, https://doi.org/10.1175/BAMS-D-18-0189.1.

Lander, M. A., 1996: Specific tropical cyclone track types and unusual tropical cyclone motions associated with a reverse-oriented monsoon trough in the western North Pacific. *Wea. Forecasting*, **11**, 170–186, https://doi.org/10.1175/1520-0434(1996)011<0170:STCTTA>2.0.CO;2.

Lee, D. Y., J.-Y. Lee, Y.-M. Yang, P.-C. Hsu, and J.-E. Kim, 2022: Dominant processes for dependence of boreal summer intraseasonal oscillation on El Niño phases. *Geophys. Res. Lett.*, **49**, e2022GL098669, https://doi.org/10.1029/2022GL098669.

Lee, J.-Y., B. Wang, M. C. Wheeler, X. Fu, D. E. Waliser, and I.-S. Kang, 2013: Real-time multivariate indices for the boreal summer intraseasonal oscillation over the Asian summer monsoon region. *Climate Dyn.*, **40**, 493–509, https://doi.org/10.1007/s00382-012-1544-4.

Lee, S.-S., B. Wang, D. E. Waliser, J. M. Neena, and J.-Y. Lee, 2015: Predictability and prediction skill of the boreal summer intraseasonal oscillation in the intraseasonal variability hindcast experiment. *Climate Dyn.*, **45**, 2123–2135, https://doi.org/10.1007/s00382-014-2461-5.

Li, S., and W. Mei, 2024: Spatiotemporal variability of tropical cyclone genesis density in the northwest Pacific. *J. Climate*, **37**, 1111–1129, https://doi.org/10.1175/JCLI-D-22-0868.1.

Li, X., Z.-Z. Hu, P. Liang, and J. Zhu, 2019: Contrastive influence of ENSO and PNA on variability and predictability of North American winter precipitation. *J. Climate*, **32**, 6271–6284, https://doi.org/10.1175/JCLI-D-19-0033.1.

Li, Y., F. Liu, and P.-C. Hsu, 2020: Modulation of the intraseasonal variability of Pacific-Japan pattern by ENSO. *J. Meteor. Res.*, **34**, 546–558, https://doi.org/10.1007/s13351-020-9182-y.

Liu, C., W. Zhang, F. Jiang, M. F. Stuecker, and Z. Huang, 2021: Record-low WNP tropical cyclone activity in early summer 2020 due to Indian Ocean warming and Madden-Julian oscillation activity. *Geophys. Res. Lett.*, **48**, e2021GL094578, https://doi.org/10.1029/2021GL094578.

Liu, F., J. Zhao, X. Fu, and G. Huang, 2018: The role of shallow convection in promoting the northward propagation of boreal summer intraseasonal oscillation. *Theor. Appl. Climatol.*, **131**, 1387–1395, https://doi.org/10.1007/s00704-017-2064-2.

Liu, P., B. Wang, K. R. Sperber, T. Li, and G. A. Meehl, 2005: MJO in the NCAR CAM2 with the tiedtke convective scheme. *J. Climate*, **18**, 3007–3020, https://doi.org/10.1175/JCLI3458.1.

Lu, R., and Z. Lin, 2009: Role of subtropical precipitation anomalies in maintaining the summertime meridional teleconnection over the western North Pacific and East Asia. *J. Climate*, **22**, 2058–2072, https://doi.org/10.1175/2008JCLI2444.1.

Mei, W., and S. Li, 2022: Variability and predictability of basin-wide and sub-basin tropical cyclone genesis frequency in the northwest Pacific. *J. Climate*, **35**, 6865–6884, https://doi.org/10.1175/JCLI-D-21-0232.1.

——, Y. Kamae, S.-P. Xie, and K. Yoshida, 2019: Variability and predictability of North Atlantic hurricane frequency in a large ensemble of high-resolution atmospheric simulations. *J. Climate*, **32**, 3153–3167, https://doi.org/10.1175/JCLI-D-18-0554.1.

Murakami, H., B. Wang, and A. Kitoh, 2011: Future change of western North Pacific typhoons: Projections by a 20-km-mesh global atmospheric model. *J. Climate*, **24**, 1154–1169, https://doi.org/10.1175/2010JCLI3723.1.

——, and Coauthors, 2015: Simulation and prediction of category 4 and 5 hurricanes in the high-resolution GFDL HiFLOR coupled climate model. *J. Climate*, **28**, 9058–9079, https://doi.org/10.1175/JCLI-D-15-0216.1.

Nitta, T., 1989: Global features of the Pacific-Japan oscillation. *Meteor. Atmos. Phys.*, **41**, 5–12, https://doi.org/10.1007/BF01032585.

Patricola, C. M., P. Chang, and R. Saravanan, 2016: Degree of simulated suppression of Atlantic tropical cyclones modulated by flavour of El Niño. *Nat. Geosci.*, **9**, 155–160, https://doi.org/10.1038/ngeo2624.

Qian, Y., P.-C. Hsu, and K. Kazuyoshi, 2019: New real-time indices for the quasi-biweekly oscillation over the Asian summer monsoon region. *Climate Dyn.*, **53**, 2603–2624, https://doi.org/10.1007/s00382-019-04644-0.

Unauthenticated | Downloaded 11/13/26 12:23 PM UTC

Roberts, M. J., and Coauthors, 2020: Impact of model resolution on tropical cyclone simulation using the HighResMIP–PRIMAVERA multimodel ensemble. *J. Climate*, **33**, 2557–2583, https://doi.org/10.1175/JCLI-D-19-0639.1.

Schreck, C. J, and Coauthors , 2023: Advances in tropical cyclone prediction on subseasonal time scales during 2019–2022. *Tropical Cyclone Research and Review*, **12**, 136–150, https://doi.org/10.1016/j.tcrr.2023.06.004.

Shen, W., J. Tang, Y. Wang, S. Wang, and X. Niu, 2017: Evaluation of WRF model simulations of tropical cyclones in the western North Pacific over the CORDEX East Asia domain. *Climate Dyn.*, **48**, 2419–2435, https://doi.org/10.1007/s00382-016-3213-5.

——, J. Song, G. Liu, Y. Zhuang, Y. Wang, and J. Tang, 2019: The effect of convection scheme on tropical cyclones simulations over the CORDEX East Asia domain. *Climate Dyn.*, **52**, 4695–4713, https://doi.org/10.1007/s00382-018-4405-y.

Showman, A. P., and L. M. Polvani, 2010: The Matsuno-Gill model and equatorial superrotation. *Geophys. Res. Lett.*, **37**, L18811, https://doi.org/10.1029/2010GL044343.

Si, S., H. Zhao, S. Chen, P. J. Klothzbach, and G. B. Raga, 2024: Evaluation of the boreal summer intraseasonal oscillation modulation on western North Pacific tropical cyclone genesis in CMIP6 HighResMIP models. *Climate Dyn.*, **62**, 10 091–10 111, https://doi.org/10.1007/s00382-024-07437-2.

Song, K., J. Zhao, R. Zhan, L. Tao, and L. Chen, 2022: Confidence and uncertainty in simulating tropical cyclone long-term variability using the CMIP6-HighResMIP. *J. Climate*, **35**, 6431–6451, https://doi.org/10.1175/JCLI-D-21-0875.1.

Tang, Y., and B. Yu, 2008: MJO and its relationship to ENSO. *J. Geophys. Res.*, **113**, D14106, https://doi.org/10.1029/2007JD009230.

Tiedtke, M., 1989: A comprehensive mass flux scheme for cumulus parameterization in large-scale models. *Mon. Wea. Rev.*, **117**, 1779–1800, https://doi.org/10.1175/1520-0493(1989)117<1779:ACMFSF>2.0.CO;2.

Trenberth, K. E., and D. J. Shea, 2006: Atlantic hurricanes and natural variability in 2005. *Geophys. Res. Lett.*, **33**, L12704, https://doi.org/10.1029/2006GL026894.

Wang, C., L. Zhang, S.-K. Lee, L. Wu, and C. R. Mechoso, 2014: A global perspective on CMIP5 climate model biases. *Nat. Climate Change*, **4**, 201–205, https://doi.org/10.1038/nclimate2118.

Wang, S., A. H. Sobel, M. K. Tippett, and F. Vitart, 2019: Prediction and predictability of tropical intraseasonal convection: Seasonal dependence and the Maritime Continent prediction barrier. *Climate Dyn.*, **52**, 6015–6031, https://doi.org/10.1007/s00382-018-4492-9.

Wang, X., S.-P. Xie, Z. Guan, and M. Wang, 2021: A common base mode of Asian summer monsoon variability across timescales. *J. Climate*, **34**, 7359–7371, https://doi.org/10.1175/JCLI-D-20-0856.1.

Wang, Y., 2001: An explicit simulation of tropical cyclones with a triply nested movable mesh primitive equation model: TCM3. Part I: Model description and control experiment. *Mon. Wea. Rev.*, **129**, 1370–1394, https://doi.org/10.1175/1520-0493(2001)129<1370:AESOTC>2.0.CO;2.

——, O. L. Sen, and B. Wang, 2003: A highly resolved regional climate model (IPRC-RegCM) and its simulation of the 1998 severe precipitation event over China. Part I: Model description and verification of simulation. *J. Climate*, **16**, 1721–1738, https://doi.org/10.1175/1520-0442(2003)016<1721:AHRRCM>2.0.CO;2.

——, M. Satoh, R. Zhan, J. Zhao, and S. Xie, 2025: Tropical sea surface warming patterns andtropical cyclone activity: A review. *Adv. Atmos. Sci.*, https://doi.org/10.1007/s00376-025-5114-1.

Wu, C.-C., R. Zhan, Y. Lu, and Y. Wang, 2012: Internal variability of the dynamically downscaled tropical cyclone activity over the western North Pacific by the IPRC Regional Atmospheric Model. *J. Climate*, **25**, 2104–2122, https://doi.org/10.1175/JCLI-D-11-00143.1.

Xiang, B., and Coauthors, 2022: S2S prediction in GFDL SPEAR: MJO diversity and teleconnections. *Bull. Amer. Meteor. Soc.*, **103**, E463–E484, https://doi.org/10.1175/BAMS-D-21-0124.1.

Yang, Y.-M., S.-I. An, B. Wang, and J. H. Park, 2020: A global-scale multidecadal variability driven by Atlantic multidecadal oscillation. *Natl. Sci. Rev.*, **7**, 1190–1197, https://doi.org/10.1093/nsr/nwz216.

Zhan, R., Y. Wang, and C.-C. Wu, 2011: Impact of SSTA in the East Indian Ocean on the frequency of northwest Pacific tropical cyclones: A regional atmospheric model study. *J. Climate*, **24**, 6227–6242, https://doi.org/10.1175/JCLI-D-10-05014.1.

——, ——, and Q. Liu, 2017: Salient differences in tropical cyclone activity over the western North Pacific between 1998 and 2016. *J. Climate*, **30**, 9979–9997, https://doi.org/10.1175/JCLI-D-17-0263.1.

Zhang, C., and Y. Wang, 2017: Projected future changes of tropical cyclone activity over the western North and South Pacific in a 20-km-mesh regional climate model. *J. Climate*, **30**, 5923–5941, https://doi.org/10.1175/JCLI-D-16-0597.1.

——, and ——, 2018: Why is the simulated climatology of tropical cyclones so sensitive to the choice of cumulus parameterization scheme in the WRF model? *Climate Dyn.*, **51**, 3613–3633, https://doi.org/10.1007/s00382-018-4099-1.

Zhang, S., H. Zhao, P. J. Klotzbach, X. Jiang, G. Chen, and S. Chen, 2023: Interannual variability in the boreal summer intraseasonal oscillation modulates the meridional migration of western North Pacific tropical cyclone genesis. *J. Climate*, **36**, 4543–4558, https://doi.org/10.1175/JCLI-D-22-0406.1.

Zhang, W., G. A. Vecchi, H. Murakami, G. Villarini, T. L. Delworth, X. Yang, and L. Jia, 2018: Dominant role of Atlantic multidecadal oscillation in the recent decadal changes in western North Pacific tropical cyclone activity. *Geophys. Res. Lett.*, **45**, 354–362, https://doi.org/10.1002/2017GL076397.

Zhao, H., R. Yoshida, and G. B. Raga, 2015: Impact of the Madden–Julian oscillation on western North Pacific tropical cyclogenesis associated with large-scale patterns. *J. Climate*, **54**, 1413–1429, https://doi.org/10.1175/JAMC-D-14-0254.1.

Zhao, J., R. Zhan, Y. Wang, and H. Xu, 2018: Contribution of the interdecadal Pacific Oscillation to the recent abrupt decrease in tropical cyclone genesis frequency over the western North Pacific since 1998. *J. Climate*, **31**, 8211–8224, https://doi.org/10.1175/JCLI-D-18-0202.1.

——, ——, H. Murakami, Y. Wang, S.-P. Xie, L. Zhang, and Y. Guo, 2023a: Atmospheric modes fiddling the simulated ENSO impact on tropical cyclone genesis over the northwest Pacific. *npj Climate Atmos. Sci.*, **6**, 213, https://doi.org/10.1038/s41612-023-00537-6.

——, M.-K. Sung, J.-H. Park, J.-J. Luo, and J.-S. Kug, 2023b: Part I observational study on a new mechanism for North Pacific Oscillation influencing the tropics. *npj Climate Atmos. Sci.*, **6**, 15, https://doi.org/10.1038/s41612-023-00336-z.

Zhao, M., I. M. Held, S.-J. Lin, and G. A. Vecchi, 2009: Simulations of global hurricane climatology, interannual variability, and response to global warming using a 50-km resolution GCM. *J. Climate*, **22**, 6653–6678, https://doi.org/10.1175/2009JCLI3049.1.

Unauthenticated | Downloaded 11/13/26 12:23 PM UTC